

# Shared Certificates for Neural Network Verification

Christian Sprecher<sup>1</sup> Marc Fischer<sup>2†</sup> Dimitar I. Dimitrov<sup>2</sup> Gagandeep Singh<sup>3</sup> Martin Vechev<sup>2</sup>

<sup>1</sup> Nostic Solutions AG\*

<sup>2</sup> ETH Zurich

<sup>3</sup> University of Illinois at Urbana-Champaign & VMware Research

christian.sprecher@nostic.ch, ggnds@illinois.edu, { marc.fischer<sup>†</sup>, dimitar.iliev.dimitrov, martin.vechev }@inf.ethz.ch

## Abstract

Existing neural network verifiers compute a proof that each input is handled correctly under a given perturbation by propagating a convex set of reachable values at each layer. This process is repeated independently for each input (e.g., image) and perturbation (e.g., rotation), leading to an expensive overall proof effort when handling an entire dataset. In this work we introduce a new method for reducing this verification cost based on the key insight that convex sets obtained at intermediate layers can overlap across different inputs and perturbations. Leveraging this insight, we introduce the general concept of shared certificates, enabling proof effort reuse across multiple inputs and driving down overall verification costs. We validate our insight via an extensive experimental evaluation and demonstrate the effectiveness of shared certificates on a range of datasets and attack specifications including geometric, patch and  $\ell_\infty$  input perturbations.

## 1 Introduction

Recent years have witnessed emerging interest in formally verifying properties of neural networks (e.g., robustness to adversarial perturbations) (Katz et al. 2017; Ehlers 2017; Bunel et al. 2018; Katz et al. 2019; Tjeng, Xiao, and Tedrake 2019; Anderson et al. 2019; Lu and Kumar 2020; Botoeva et al. 2020; Dvijotham et al. 2018; Wong and Kolter 2018; Gehr et al. 2018; Singh et al. 2018a; Raghunathan, Steinhardt, and Liang 2018; Singh et al. 2019; Zhang et al. 2018; Dvijotham et al. 2019; Weng et al. 2018; Salman et al. 2019; Wang et al. 2018; Mohapatra et al. 2020). Conceptually, existing verifiers work by propagating sets of inputs captured in symbolic form (such as a convex sets) through the network, an expensive process which produces relaxations of all possible activations at intermediate layers. We illustrate the process in Fig. 1a where an input shape (orange square around a data point) is propagated from left to right, obtaining intermediate shapes on the way (here the goal is to verify all points in the input region are classified as “cat”). The key technical challenge all existing verifiers aim to address is speeding up and scaling the certification process (i.e, faster and more efficient propagation of symbolic shapes, while ensuring sufficient precision of these shapes.

\*work performed while at ETH Zurich

<sup>†</sup>primary contact

Preprint. Under review.

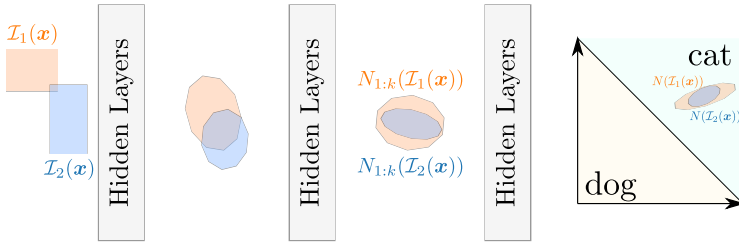
## This work: accelerating certification via proof sharing

In this work we propose a new, complementary method for accelerating neural network verification based on the key observation that instead of treating each certification attempt in isolation as existing verifiers do, we can reuse proof effort among multiple such attempts, thus obtaining significant overall speed-ups.

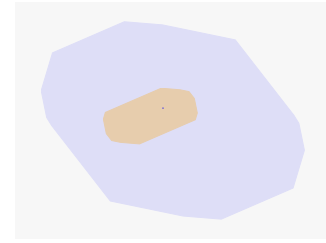
We illustrate the concept in Fig. 1a. First, as standard, the verifier produces convex sets at intermediate layers (e.g., orange shapes), forming a *proof* of the property (e.g., robustness). Then, we observe that the relaxations (convex sets) for a new proof attempt (e.g., blue shapes) can be contained inside existing relaxations from another proof, an effect we term *proof subsumption*. This effect can be observed both between relaxations obtained from different specifications (e.g.,  $\ell_\infty$  and adversarial patches) for the same data point and it can also be observed between proofs for the same property but different, yet semantically similar inputs. Building on this observation we introduce the notion of proof sharing via templates. Proof sharing works in two steps: first we leverage relaxations from existing proofs in order to create templates, and second, we augment the verifier with these templates, stopping the expensive propagation at an intermediate layer as soon as the newly generated relaxation is included inside a template. Key technical ingredients to the effectiveness of our approach are fast template generation and inclusion checking techniques. We experimentally demonstrate that proof sharing can achieve significant speed-ups in important verification scenarios including proving robustness to adversarial patches (Chiang et al. 2020) and geometric perturbations (Balunovic et al. 2019).

**Main Contributions** Our key contributions are:

- An introduction and formalization of the concept of proof sharing in neural network verification: the idea that some proofs capture others.
- A framework leveraging the above concept, enabling proof effort reuse via proof templates.
- A thorough experimental evaluation involving verification of robustness to adversarial patch, geometric and  $\ell_\infty$  perturbations, demonstrating templates with proof match rates of up 95% as well as non-trivial end-to-end certification speed-ups.



(a) Visualization of neural network verification. High-dimensional convex shapes (visualized in 2d) are propagated layer by layer.



(b) The relaxation (box abstraction) obtained for  $\mathcal{I}_\epsilon(\mathbf{x})$  (blue) contains that for  $\mathcal{I}_p^{i,j}(\mathbf{x})$  (adversarial patch; orange) (projected down to 2d).

Figure 1: Some proofs imply others: Fig. 1a shows neural network verification, where input regions  $\mathcal{I}_1(\mathbf{x}), \mathcal{I}_2(\mathbf{x})$  are propagated layer by layer through a neural network  $N$ . While initially  $\mathcal{I}_1(\mathbf{x})$  and  $\mathcal{I}_2(\mathbf{x})$  only slightly overlap, at layer  $k$ ,  $N_{1:k}(\mathcal{I}_2(\mathbf{x}))$  is fully contained in  $N_{1:k}(\mathcal{I}_1(\mathbf{x}))$ . Fig. 1b shows this in a real classifier for the MNIST dataset. For details see §3 and App. A.2.

We believe that because proof sharing is a widely applicable concept which is also orthogonal to existing verification techniques, it can trigger future research instantiating the idea to different networks, datasets and certification methods, as well as drive interesting theoretical investigations for why proof sharing is indeed possible (e.g., similar to the idea of transferrability of adversarial examples (Papernot, McDaniel, and Goodfellow 2016)).

## 2 Related Work

Next, we briefly discuss conceptually related work: Ashok et al. (2020) simplify neural networks before applying verification algorithms to achieve speed-ups. This simplification is conducted in a way that the obtained proof can be adapted to the original neural network. Similarly, Zhong et al. (2021) replace blocks neural networks with summaries in order to speed up verification. Paulsen, Wang, and Wang (2020); Paulsen et al. (2020) analyzes the difference between two closest related neural networks, exploring their structural similarity in the analysis. Cheng and Yan (2021) reuse previous analysis results after a neural network is slightly modified, e.g. fine-tuned. In a temporal setting, Wei and Liu (2021) utilize verification results from previous time-steps to seed the verification at the next time-step, allowing faster adaptation to changes in inputs and the neural network.

In contrast to these works, we do not modify the neural network, but achieve speed-ups rather by only considering the convex relaxations obtained in the proofs.

## 3 Proof Sharing with Templates

We now introduce our formal framework of proof sharing. We consider a network  $N : \mathbb{R}^m \rightarrow \mathbb{R}^n$  composed of  $L$  layers. For  $k < L$ , we let  $N_{1:k}$  denote the first  $k$  layers and  $N_{k+1:L}$  denote the last  $L - k$  layers. We treat the neural network  $N$  as well as  $N_{1:k}$  and  $N_{k+1:L}$  as a function applicable to both individual points as well as regions.

**Background: Neural Network Verification** To this end we first briefly review the necessary background on neural network verification. Robustness verification is an instance of local verification: proving a property  $\psi$  holds for a given

region  $\mathcal{I}(\mathbf{x})$  formed around the input  $\mathbf{x}$ . The problem is formally stated as follows:

**Problem 1 (Local neural network verification)** For a region  $\mathcal{I}(\mathbf{x})$  around an input  $\mathbf{x}$ , neural network  $N$ , and post-condition  $\psi$  verify that  $\forall \mathbf{z} \in \mathcal{I}(\mathbf{x}). N(\mathbf{z}) \vdash \psi$ .

To tackle this problem, existing verifies propagate  $\mathcal{I}(\mathbf{x})$  through the network  $N$ , resulting in a relaxation at each layer, finally checking if the output relaxation implies  $\psi$ . This is showcased in Fig. 1a, where the shapes  $\mathcal{I}_1(\mathbf{x})$  and  $\mathcal{I}_2(\mathbf{x})$  are propagated layer-by-layer through the neural network  $N$ . In the case of robustness verification, where one tries to prove classification invariance to adversarial examples (Szegedy et al. 2014; Biggio et al. 2013), a common input region is the  $\ell_\infty$ -bounded additive noise, defined as  $\mathcal{I}_\epsilon(\mathbf{x}) := \{\mathbf{z} \mid \|\mathbf{x} - \mathbf{z}\|_\infty \leq \epsilon\}$ . Here,  $\epsilon$  defines the size of the maximal perturbation to  $\mathbf{x}$ , while  $\psi$  denotes classification to the same class as  $\mathbf{x}$ . Throughout this paper, we consider different instantiations for  $\mathcal{I}(\mathbf{x})$  but assume that  $\psi$  denotes classification invariance (although other choices would work analogously). In Fig. 1a, we can verify that all point contained in  $N(\mathcal{I}_1(\mathbf{x}))$  are classified as “cat”.

Exact verification (Tjeng, Xiao, and Tedrake 2019) can propagate exact sets rather than relaxations. However, to express them in tractable form it is necessary to relax their representation. Thus we use the term “relaxation” throughout.

**Motivation: Proof Subsumption** Empirically we found that for many input regions  $\mathcal{I}_i(\mathbf{x})$  and  $\mathcal{I}_j(\mathbf{x})$  we have  $N_{1:k}(\mathcal{I}_i(\mathbf{x})) \subseteq N_{1:k}(\mathcal{I}_j(\mathbf{x}))$  for some intermediate layer  $k$  even though  $\mathcal{I}_i(\mathbf{x}) \not\subseteq \mathcal{I}_j(\mathbf{x})$ . We refer to this property as proof subsumption. The property is showcased in Fig. 1a, where  $\mathcal{I}_1(\mathbf{x})$  and  $\mathcal{I}_2(\mathbf{x})$  have only small overlap, yet  $N_{1:k}(\mathcal{I}_2(\mathbf{x})) \subseteq N_{1:k}(\mathcal{I}_1(\mathbf{x}))$ .

Before building upon this we now showcase proof subsumption on a real verification task. To this end we consider adversarial patches (Chiang et al. 2020), letting  $\mathcal{I}_p^{i,j}$  denote an input region obtained by placing a  $2 \times 2$  patch at position  $(i, j)$  on the input image  $\mathbf{x}$  (arbitrary changes to pixel intensity are allowed inside the patch). Further, we consider a feed-forward neural network classifier (details in App. A.2) for the classification of the MNIST (LeCun et al. 1989) dataset. The accuracy and verified accuracy for  $\mathcal{I}_\epsilon$

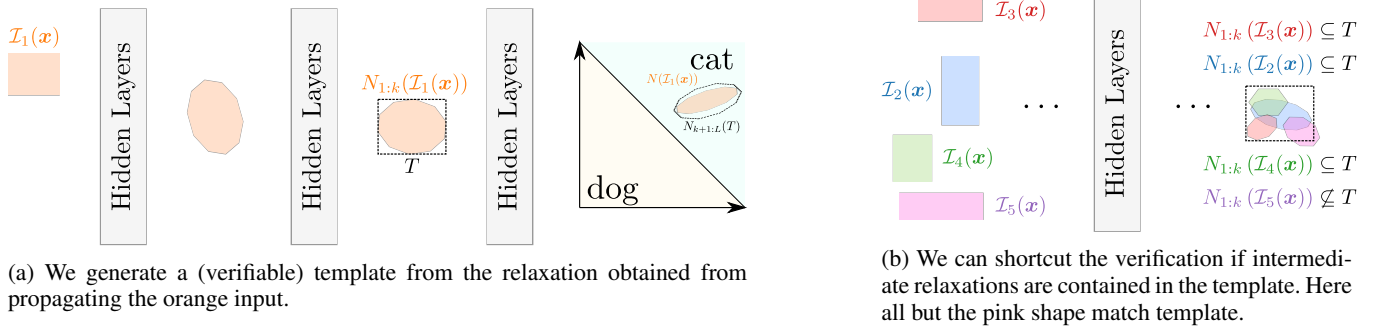


Figure 2: Conceptualization of proof sharing with templates. In Fig. 2a we create a verifiable template  $T$  (black-dashed border) from the relaxation of the orange specification  $N_{1:k}(\mathcal{I}_1(\mathbf{x}))$ . When verifying new specifications  $\mathcal{I}_2 \dots \mathcal{I}_5$ , shown in Fig. 2b, we can shortcut the verification once we have established that the intermediate relaxations are contained in the template.

with  $\epsilon = 0.1$  and  $0.2$  of this classifier of the test set is given in Table 1. For 1000 inputs  $\mathbf{x}$  for which  $\mathcal{I}_\epsilon(\mathbf{x})$  is verifiable we sample two random patch locations  $(i, j)$  each and also propagate  $\mathcal{I}_p^{i,j}(\mathbf{x})$  through the network and denote the percentage of  $\mathcal{I}_p^{i,j}(\mathbf{x})$  contained in  $\mathcal{I}_\epsilon(\mathbf{x})$  at layer  $k$ . We visualize the case where a patch relaxation  $\mathcal{I}_p^{i,j}(\mathbf{x})$  (in orange) is contained within the  $\ell_\infty$  relaxation  $\mathcal{I}_\epsilon$  (in blue) in Fig. 1b. For further experimental details as well as results on a convolutional network see App. A.2.

We observe that regions with larger  $\epsilon$  yield more inclusions. Further we observe that the containment increases as  $k$  increases. These two observations give an intuitions as why we observe proof subsumption. As relaxations pass through the neural network, in each layer the relaxations become more imprecise. While this fundamentally limits verification, it makes subsumption of relaxations more probable. Further, while passing through the layers of a neural network, we observed that semantically similar (yet distinct) image inputs have activation vectors that grow closer in  $\ell_2$  norm as they pass through the layers of the neural network (Krizhevsky, Sutskever, and Hinton 2012; Szegedy et al. 2014). We conjecture that these two effects are driving the observed proof subsumption. As larger  $\epsilon$  also increases the size of the obtained relaxations for an  $\ell_\infty$ -perturbation, they also increase the rate of other relaxations matching them.

**Proof Sharing with Templates** Leveraging this insight, we introduce the idea of proof sharing via templates, showcased in Fig. 2. There we use a relaxation obtained from a robustness proof  $N_{1:k}(\mathcal{I}_1(\mathbf{x}))$  at layer  $k$  to create a template  $T$ . After ensuring that  $T$  is verifiable, it can be used to shortcut the evaluation of further proofs, e.g., of  $\mathcal{I}_2(\mathbf{x}), \dots, \mathcal{I}_5(\mathbf{x})$ .

Formally we decompose this into two sub-problems: the generation of proof templates and the matching of relaxations corresponding to other properties to these templates.

Our goal in proof sharing is to construct a suitable template  $T$  at layer  $k$  by using the relaxations produced by the verification procedure, so that  $T$  captures further relaxation at layer  $k$  obtained from propagating unseen  $\mathcal{I}(\mathbf{x})$ , yet still ensure that  $T$  verifies. As it can be challenging to capture all input regions with a single  $T$ , we allow a set of templates  $\mathcal{T}$ . Finding a set of templates is formally stated as:

$\epsilon$	verif. acc. [%]	$\mathcal{I}_p(\mathbf{x}) \subseteq \mathcal{I}_\epsilon(\mathbf{x})$ at layer $k$ [%]				
		1	2	3	4	5
0.1	89.74	61.40	72.85	77.65	81.75	82.70
0.2	81.40	62.85	77.05	82.40	86.05	86.60

Table 1: Proof subsumption on a robust MNIST classifier with 94 % accuracy. Verif. acc. denotes the percentage of verifiable inputs from the test set for  $\ell_\infty$ -perturbations ( $\mathcal{I}_\epsilon$ ).

**Problem 2 (Template Generation)** For a given neural network  $N$ , layer  $k$  and a postcondition  $\psi$ , find a set of templates  $\mathcal{T}$  with  $|\mathcal{T}| \leq m$  such that:

$$\max_{\mathcal{T}} \mathbb{E}_{(\mathbf{x}, \mathcal{I}) \sim \mathcal{P}} \left[ \bigvee_{T \in \mathcal{T}} N_{1:k}(\mathcal{I}(\mathbf{x})) \subseteq T \right] \quad (1)$$

s.t.  $\forall T \in \mathcal{T}. N_{k+1:L}(T) \vdash \psi$

Problem 2 is deliberately general in order to admit different instantiations. In particular,  $\mathcal{P}$  denotes the distribution of expected input regions defined by  $\mathbf{x}$  and  $\mathcal{I}$ . This formulation allows for various scenarios including  $\mathbf{x}$  and  $\mathcal{I}$  to be jointly distributed, but also for a fixed  $\mathcal{I}$  and a  $\mathbf{x}$  drawn from a data distribution  $\mathcal{D}$ , as well as a fixed  $\mathbf{x}$  and a  $\mathcal{I}$  drawn from a set of possible specifications. Further the formulation does not specify which convex relaxations are used to represent  $T$  and to propagate  $\mathcal{I}(\mathbf{x})$  and  $T$  through  $N_{1:k}$  and  $N_{k+1:L}$ .

Problem 2 does not necessarily require that the templates  $T$  are created from previous proofs. However, using our observation from the motivation section, in §4 we will infer the templates from previously obtained relaxations.

To leverage proof sharing once the templates  $\mathcal{T}$  are obtained, we need to be able to match a relaxation  $S = N_{1:k}(\mathcal{I}(\mathbf{x}))$  to a template in  $\mathcal{T}$ :

**Problem 3 (Template Matching)** Given a set of templates  $\mathcal{T}$  at layer  $k$  of a neural network  $N$ , and a new input region  $\mathcal{I}(\mathbf{x})$ , determine whether there exists a  $T \in \mathcal{T}$  such that  $S \subseteq T$ , where  $S = N_{1:k}(\mathcal{I}(\mathbf{x}))$ .

Together, Problems 2 and 3 outline a general framework for proof sharing, permitting many instantiations. We note

that Problems 2 and 3 present an inherent precision vs. speed trade-off: Problem 3 can be solved most efficiently for small values of  $m = |\mathcal{T}|$  and simpler representations of  $T$  (allowing faster checking of  $S \subseteq T$ ). Alternatively, Eq. (1) can be maximized by large  $m$  and  $T$  represented by complex relaxations, thus attaining high precision.

**Beyond proof sharing on the same input** We focus on proof sharing for different specifications on the same input  $\mathbf{x}$ . However, we observed that proof sharing is even possible between different inputs  $\mathbf{x}$  and  $\mathbf{x}'$ . This further highlights the connection to abstraction property of neural networks, that causes semantically similar inputs to have similar activation vectors (Krizhevsky, Sutskever, and Hinton 2012; Szegedy et al. 2014). We discuss this in App. B. There, we also discuss the creation of templates for proof sharing in an offline setting from the training set, with the aim of speeding up the verification of new inputs. This allows for different trade-offs (e.g., more expensive template generation) and highlights the generality of the proposed framework. In fact, we show in §5.3 that for MNIST we can create a set of templates from the training set that can capture 60% specifications over previously unseen test set inputs. This enables speeding up the verification of unseen inputs.

## 4 Online Template Generation

We now consider an instantiation of proof sharing, where we are given an input  $\mathbf{x}$  and properties  $\mathcal{I}_1, \dots, \mathcal{I}_r$  to verify. To formalize this setting, we instantiate Problem 2, for a distribution  $\mathcal{P}$ , over a single fixed  $\mathbf{x}$  and  $\mathcal{I}_1, \dots, \mathcal{I}_r$ . The procedure utilizing proof sharing is outlined in Algorithm 1. There, we first create the set of templates  $\mathcal{T}$  and subsequently verify  $\mathcal{I}_1, \dots, \mathcal{I}_r$  using  $\mathcal{T}$ . From this outline it is clear that in order to achieve a noticeable speedup it is paramount for  $\mathcal{T}$  to match many relaxations,  $k$  to be low, the template generation (line 1) as well as the template matching (line 6) to be fast.

To achieve this we first discuss the choice of relaxation to be used in the propagation and representation of the templates. Then we discuss the template generation procedure, and instantiate it for the verification of robustness to adversarial patches and geometric perturbations in §4.1 and §4.2.

**Choice of Relaxation** As noted earlier, the choice of how to represent the templates leads to a trade-off between Problems 2 and 3. We briefly outline two common choices for convex relaxations used in neural network verification and how they are suited to these problems: the Box and Zonotope relaxations (Gehr et al. 2018; Singh et al. 2018b; Wong and Kolter 2018; Mirman, Gehr, and Vechev 2018). A  $d$ -dimensional box is described as

$$B = \{\mathbf{a} + \text{diag}(\mathbf{d})\mathbf{e} \mid \mathbf{e} \in [-1, 1]^d\},$$

parametrized by a center  $\mathbf{a} \in \mathbb{R}^d$  and width  $\mathbf{d} \in \mathbb{R}_{\geq 0}^d$ . A Zonotope  $Z$  is of the form

$$S = \{\mathbf{a} + \mathbf{A}\mathbf{e} \mid \mathbf{e} \in [-1, 1]^p\},$$

parametrized with  $\mathbf{a} \in \mathbb{R}^d$  and  $\mathbf{A} \in \mathbb{R}^{d \times p}$ .

While not a formal hierarchy, Zonotopes generally are more precise, e.g. include less superfluous points in the intermediate relaxations, allowing for higher verified accuracy.

However, for a Zonotope  $T$  the inclusion check  $S \subseteq T$  is computationally expensive (Sadraddini and Tedrake 2019) regardless of how  $S$  is represented (unless parameters are trivial or heavily constrained). Yet for a box  $T$  this check can be done easily. We thus propagate Zonotopes through the neural network and represent the templates  $T$  as boxes. As is obvious by our choice of notation, any box  $B$  is a special case of a Zonotope, but the reverse is not true. However, for a Zonotope  $Z$  its tight bounding box  $B_Z = \alpha(Z)$  can be easily obtained. The center of  $B_Z$  is  $\mathbf{a}$ , the center of  $Z$ . The width  $\mathbf{d} \in \mathbb{R}_{\geq 0}^d$  is given as  $\mathbf{d}_i = \sum_{j=1}^p |A_{i,j}|$ . To check  $B_1 \subseteq B_2$  for two boxes, we can simply check  $\bigwedge_{i=1}^d \mathbf{a}_i^2 - \mathbf{d}_i^2 \leq \mathbf{a}_i^1 - \mathbf{d}_i^1 \wedge \mathbf{a}_i^1 + \mathbf{d}_i^1 \leq \mathbf{a}_i^2 + \mathbf{d}_i^2$ . To check  $Z \subseteq B$ , for a Zonotope  $Z$  and box  $B$  it suffices to check  $\alpha(Z) \subseteq B$ .

**Template Generation** Following the insight that intermediate relaxations for some perturbations include those of others, we slightly relax the problem in order to create  $m$  templates  $T_i$  from intermediate relaxations  $N_{1:k}(\hat{\mathcal{I}}_i(\mathbf{x}))$  for some  $\hat{\mathcal{I}}_1, \dots, \hat{\mathcal{I}}_m$ . We reiterate, that we write  $N_{1:k}(\hat{\mathcal{I}}_i(\mathbf{x}))$  for the propagation  $\hat{\mathcal{I}}_i$  by the verifier up to layer  $k$ . Further, we let  $\mathcal{P}_{\mathcal{I}}$  denote the categorical distribution over  $\mathcal{I}_1, \dots, \mathcal{I}_r$ , the  $r$  specifications we aim to verify. We note that the  $\hat{\mathcal{I}}_i$  are not directly related to  $\mathcal{I}_1, \dots, \mathcal{I}_r$ . Then, for a particular layer  $k$ , image  $\mathbf{x}$  and number of templates  $m$  we optimize

$$\arg \max_{\hat{\mathcal{I}}_1, \dots, \hat{\mathcal{I}}_m} \mathbb{E}_{\mathcal{I} \sim \mathcal{P}_{\mathcal{I}}} \left[ \bigvee_{i=1}^m N_{1:k}(\mathcal{I}(\mathbf{x})) \subseteq T_i \right] \quad (2)$$

$$\text{where } T_i = \alpha(N_{1:k}(\hat{\mathcal{I}}_i(\mathbf{x})))$$

$$\text{s.t. } N_{k+1:L}(T_i) \vdash \psi \text{ for } i \in 1, \dots, m.$$

This problem is solved by selecting  $\hat{\mathcal{I}}_1, \dots, \hat{\mathcal{I}}_m$  such that the resulting templates cover as much as possible of the relaxations obtained from propagating  $\mathcal{I} \sim \mathcal{P}_{\mathcal{I}}$ . To this end, in §4.1 and §4.2 we will choose parametric  $\hat{\mathcal{I}}_i$  and solve Eq. (2) by optimizing over these parameters. Note, the templates are boxes obtained from the Zonotope propagation via  $\alpha$ .

### 4.1 Robustness to Adversarial Patches

We now instantiate the above scheme in order to verify robustness against adversarial patches in image classification (Chiang et al. 2020). Consider an attacker that is allowed to arbitrarily change any  $p \times p$  patch of the image. For such a patch over pixel positions  $([i, i+p-1] \times [j, j+p-1])$ , the corresponding perturbation is

$$\mathcal{I}_{p \times p}^{i,j}(\mathbf{x}) := \{\mathbf{z} \in [0, 1]^{h \times w} \mid \forall (k, l) \in \pi_{p \times p}^{i,j} \quad \mathbf{z}_{k,l} = \mathbf{x}_{k,l}\}$$

$$\text{where } \pi_{p \times p}^{i,j} = \left\{ (k, l) \mid \begin{array}{l} k \in \{1, \dots, h\} \\ l \in \{1, \dots, w\} \end{array} \right\} \setminus \left\{ (k, l) \mid \begin{array}{l} k \in \{i, \dots, i+p-1\} \\ l \in \{j, \dots, j+p-1\} \end{array} \right\}$$

and  $h$  and  $w$  denote the height and width of  $\mathbf{x}$ . To prove robustness for an arbitrarily placed  $p \times p$  patch, however, one must consider the perturbation set  $\mathcal{I}_{p \times p}(\mathbf{x}) := \bigcup_{i,j} \mathcal{I}_{p \times p}^{i,j}(\mathbf{x})$ .

To prove robustness for  $\mathcal{I}_{p \times p}$ , Chiang et al. (2020) separately verifies  $\mathcal{I}_{p \times p}^{i,j}(\mathbf{x})$  for all  $i \in \{1, \dots, h-p+1\}, j \in \{1, \dots, w-p+1\}$ . For example, with  $p = 2$  and a  $28 \times 28$  MNIST image, this approach requires 729 individual proofs.

---

**Algorithm 1: Online Neural Network Verification Utilizing Proof Sharing with Templates**


---

**Input:**  $\mathbf{x}, \mathcal{I}_1, \dots, \mathcal{I}_r, k, \psi$   
**Result:**  $v_1, \dots, v_r$  indicating  $v_i := (N(\mathcal{I}_i(\mathbf{x})) \vdash \psi)$

```

1  $\mathcal{T} \leftarrow \text{generate\_templates}(\mathbf{x}, N, k, \psi)$ 
2  $v_1, \dots, v_r \leftarrow \text{False}$ 
3 for  $i \leftarrow 1$  to  $r$  do
4    $S \leftarrow N_{1:k}(\mathcal{I}_i(\mathbf{x}))$ 
5   for  $T_j \in \mathcal{T}$  do
6     if  $S \subseteq T_j$  then
7        $v_i \leftarrow \text{True}$ 
8       break
9     end
10  end
11  if  $\neg v_i$  then
12     $v_i \leftarrow (N_{k+1:L}(S) \vdash \psi)$ 
13  end
14 end
15 return  $v_1, \dots, v_r$ 

```

---

Because the different proofs for  $\mathcal{I}_{p \times p}$  share similarities, one can apply proof sharing. We can utilize Algorithm 1 and check  $\bigwedge_i v_i$  at the end to speed up this process. For template generation, we solve Eq. (2) for  $m$  templates with an input perturbation  $\hat{\mathcal{I}}_i$  per template. We empirically find that choosing the  $\hat{\mathcal{I}}_i$  to be the  $\ell_\infty$ -templates  $\mathcal{I}_{\epsilon_i}$  with maximal verifiable  $\epsilon_i$  captures the patch perturbations  $\mathcal{I}_{p \times p}^{i,j}$  well. This aligns with our observations from §3. To further improve upon this, we consider  $m$  template perturbations of the form

$$\hat{\mathcal{I}}_i(\mathbf{x}) := \{z \mid \|\mathbf{x}_{\mu_i} - z_{\mu_i}\|_\infty \leq \epsilon_i\},$$

where  $\mu_i$  denotes a subset of pixels of the input image. In particular, we consider  $\mu_1, \dots, \mu_m$ , such that they partition the set of pixels in the image (e.g., in Fig. 3)

Thus, we recast the template generation in Eq. (2) as:

$$\arg \max_{\substack{\mu_1, \dots, \mu_m \\ \epsilon_1, \dots, \epsilon_m}} \mathbb{E}_{\mathcal{I} \sim \mathcal{P}_{\mathcal{I}}} \left[ \bigvee_{i=1}^m N_{1:k}(\mathcal{I}(\mathbf{x})) \subseteq T_i \right] \quad (3)$$

where  $T_i = \alpha(N_{1:k}(\hat{\mathcal{I}}_i(\mathbf{x})))$

s.t.  $N_{k+1:L}(T_i) \vdash \psi$  for  $i \in 1, \dots, m$ .

As noted, this generation procedure needs to be fast, yet obtain  $\mathcal{T}$  to which many relaxations match in order to obtain speedups. Thus, we consider small  $m$ , and fixed patterns  $\mu_1, \dots, \mu_m$ . For each  $\hat{\mathcal{I}}_i$  we then find the largest  $\epsilon_i$  in order to maximize the number of matches, which can still be verified. Note that for  $m = 1$  this is equivalent to the  $\ell_\infty$  input perturbation  $\mathcal{I}_\epsilon$  with the maximal verifiable  $\epsilon$  for the given image. Concretely, we perform binary search over  $\epsilon_i$  in order to maximize it while still satisfying  $N_{k+1:L}(\alpha(N_{1:k}(\hat{\mathcal{I}}_i))) \vdash \psi$ , where the specification is propagated as a Zonotope, converted into a box and then propagated as a Zonotope again in order to verify  $\psi$ . Formally, verifying  $\mathcal{I}_\epsilon$  with Zonotopes is not monotonous in  $\epsilon$ , making it hard to truly maximize  $\epsilon$ . This renders the application of

---

**Algorithm 2: Online Template Generation**


---

**Input:**  $\mathbf{x}, N, \mu_1, \dots, \mu_m, k_1, \dots, k_n, \psi$   
**Result:**  $\mathcal{T}^{k_1}, \dots, \mathcal{T}^{k_n}$

```

1  $\mathcal{T}^{k_1}, \dots, \mathcal{T}^{k_n} \leftarrow \{\}, \dots, \{\}$ 
2 for  $i \leftarrow 1$  to  $m$  do
3    $\hat{\mathcal{I}}_i(\epsilon) := \{z \mid \|\mathbf{x}_{\mu_i} - z_{\mu_i}\| \leq \epsilon\}$ 
4    $\epsilon_i \leftarrow \text{bin\_search}(\epsilon, N(\hat{\mathcal{I}}_i(\epsilon)) \vdash \psi)$ 
5   for  $j \leftarrow 1$  to  $n$  do
6      $T_{k_j} \leftarrow \alpha(N_{1:k_j}(\hat{\mathcal{I}}_i(\epsilon_i)))$ 
7      $T(\beta) := \beta T_{k_j}$ 
8      $\beta_{k_j} \leftarrow \text{bin\_search}(\beta, N_{k_j+1:L}(T(\beta)) \vdash \psi)$ 
9      $\mathcal{T}^{k_j} \leftarrow \mathcal{T}^{k_j} \cup \{T(\beta_{k_j})\}$ 
10  end
11 end
12 return  $\mathcal{T}^{k_1}, \dots, \mathcal{T}^{k_n}$ 

```

---

binary search a best-effort approximation. Yet, as we don't require a formal maximum but rather aim to solve a surrogate for Eq. (3), this still works well in practice.

**Templates at multiple layers** This approach can be slightly extended, yielding templates at multiple layers without a large increase in computational cost. Formally, we instantiate Eq. (3) for multiple values of  $k$  at once.

With templates at layers  $k$  and  $k'$  (with  $k \leq k'$ ) we first try to match the propagated shape against templates at layer  $k$  and if this fails, we propagate it further to layer  $k'$  and again try to match the proof. In Algorithm 1, this means repeating the block from line 4 to line 10 for each value of  $k$  before going on to the check on line 11.

The full template generation procedure is given in Algorithm 2. For each set of pixels  $\mu_i$ , best-effort maximization is applied to find to  $\epsilon_i$  while maintaining verifiability (line 4). Then for each layer  $k_j$  at which we are creating templates we obtain a box  $T_{k_j}$  from the Zonotope. As this  $T_{k_j}$  may not be verifiable we then perform another binary search for the largest scaling factor  $\beta$  such that the scaled box template becomes verifiable. Formally we scale a box  $B = \{\mathbf{a} + \text{diag}(\mathbf{d})\mathbf{e} \mid \mathbf{e} \in [-1, 1]^d\}$  by a scalar  $\beta$  is as

$$\beta B = \{\mathbf{a} + \beta \text{diag}(\mathbf{d})\mathbf{e} \mid \mathbf{e} \in [-1, 1]^d\}.$$

With well initialized binary searches this procedure can be very fast. While we don't utilize verification using box propagation in this paper, we note that for it  $\alpha$  can be replaced by the identity and the second search over  $\beta$  be skipped.

## 4.2 Geometric Robustness

Geometric robustness verification (Pei et al. 2017; Singh et al. 2019; Balunovic et al. 2019; Mohapatra et al. 2020; Li et al.; Fischer, Baader, and Vechev 2020) aims to verify robustness to geometric transformations such as image rotations or image translations. These transformations typically include an interpolation operation. We demonstrate this on the example of a rotation  $R_\gamma$  by  $\gamma \in \Gamma$  degrees for an interval  $\Gamma$  (e.g.,  $\gamma \in [-5, 5]$ ), for which we consider the perturbation  $\mathcal{I}_\Gamma(\mathbf{x}) := \{R_\gamma(\mathbf{x}) \mid \gamma \in \Gamma\}$ . We note that unlike

	shapes matched to template at layer [%]							patch verif. [%]
	$k$	1	2	3	4	5	6	
MNIST	18.6	85.6	94.1	95.2	95.5	95.7	95.7	97.0
CIFAR	0.1	27.1	33.7	34.4	34.2	34.2	34.3	42.2

	verification time [s]									
	$k$	-	1	2	3	4	1+3	2+3	2+4	2+3+4
MNIST	2.10	1.94	1.15	1.22	1.41	1.27	<b>1.09</b>	1.10	1.14	1.14
CIFAR	3.27	2.98	2.53	2.32	2.47	2.35	2.49	<b>2.42</b>	2.55	2.55

Table 2:  $\mathcal{I}_{2 \times 2}$  patch verification for different combinations of template layers  $k$ , 7x200 networks, using  $m = 1$  template.

Method/Mask	$m$	patch matched [%]	$t$ [s]
Baseline	-	-	2.14
L-infinity	1	94.1	<b>1.11</b>
Center + Border	2	94.6	1.41
2x2 Grid	4	<b>95.0</b>	3.49

Table 3:  $\mathcal{I}_{2 \times 2}$  patch verification with templates at the 2nd & 3rd layer of the 7x200 networks for different masks.

$\ell_\infty$  and patch verification, the input regions for geometric transformations are non-linear and have no closed-form solutions. Thus, an overapproximation of the input region is obtained (Balunovic et al. 2019). For large  $\Gamma$ , the approximate input region  $\mathcal{I}_\Gamma(\mathbf{x})$ , can be too coarse resulting in imprecise verification. Hence, in order to assert  $\psi$  on  $\mathcal{I}_\Gamma$ , existing state-of-the-art approaches, e.g., Balunovic et al. (2019), split  $\Gamma$  into  $r$  smaller ranges  $\Gamma_1, \dots, \Gamma_r$  and then verify  $(\mathcal{I}_{\Gamma_i}, \psi)$  for  $i \in 1, \dots, r$ . These smaller perturbations share similarities facilitating proof sharing. We instantiate our approach similar to §4.1. A key difference to §4.1 is that while there are  $\mathbf{x} \in \mathcal{I}_{p \times p}^{i,j}(\mathbf{x})$  for all  $i, j$ , here in general  $\mathbf{x} \notin \mathcal{I}_{\Gamma_i}(\mathbf{x})$  for most  $i$ . Therefore, the individual perturbations  $\mathcal{I}_i(\mathbf{x})$  do not overlap. To account for this, we consider  $m$  templates and split  $\Gamma$  into  $m$  equally sized chunks (unrelated to the  $r$  splits) obtaining the angles  $\gamma_1, \dots, \gamma_m$  at the center of each chunk. For  $m$  templates we then consider the perturbations  $\hat{\mathcal{I}}_i := \mathcal{I}_{\epsilon_i}(R_{\gamma_i}(\mathbf{x}))$ , denoting the  $\ell_\infty$  perturbation of size  $\epsilon_i$  around the  $\gamma_i$  degree rotated  $\mathbf{x}$ . To find the template we employ a procedure analogous to Algorithm 2.

## 5 Experimental Evaluation

We now experimentally evaluate the effectiveness of our algorithms from §4. We consider the verification of robustness to adversarial patch attacks and geometric transformations in §4.1 and §5.2, respectively. Additionally in §5.3, we discuss results in the setting where templates are created offline.

We define specifications on 100 images each from the MNIST (LeCun et al. 1989) and the CIFAR dataset (Krizhevsky, Hinton et al. 2009). We use Zonotope propagation as the baseline and for the propagation of relaxations

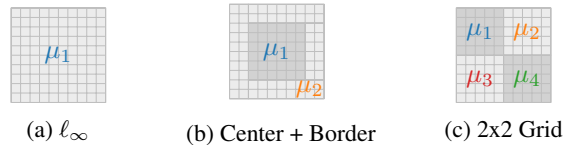


Figure 3: Template splits  $\mu$  on a  $10 \times 10$  pixel grid.

(Singh et al. 2018b). For both datasets we consider a 7 layer neural network with 200 neurons per layer, 7x200 as well as 9x500 which has 9 layers of 500 neurons. We provide further details in App. C. We implemented our algorithms in PyTorch (Paszke et al. 2019) and ran our experiments on Ubuntu 18.04 with an Intel Core i9-9900K CPU and 64 GB RAM. For all timing results we provide the mean over three runs and their standard deviation in App. D.

### 5.1 Robustness against adversarial patches

For the MNIST dataset containing  $28 \times 28$  images, as outlined in §4.1, in order to verify inputs to be robust against  $2 \times 2$  patch perturbations, 729 individual perturbations must be verified. Only if all of these are verified, the overall property can be verified for a given image. Similarly, for CIFAR, containing  $32 \times 32$  color images, there are 961 perturbations to be verified. (The patch is applied over all color channels.)

We now investigate the two main parameters of Algorithm 2: the masks  $\mu_1, \dots, \mu_m$  and the layers  $k_1, \dots, k_n$ .

We first study the impact of the layer  $k$  used for creating the template. To this end we consider the 7x200 networks, use  $m = 1$  (covering the whole image; equivalent to  $\mathcal{I}_\epsilon$ ). Table 2 shows the corresponding template matching rates, the overall percentage of individual patches that can be verified “patches verif.” (not the percentage of images for which  $\mathcal{I}_{2 \times 2}$  is true; see Table 4 as “verf.”) and verification times (including the template generation) respectively. We observe that many template matches can already be made at the second or third layer. We find that in terms of verification time, creating templates simultaneously at the second and third layer, using the method outlined in §4.1, works best overall. Thus, for further experiments we use these two layers.

Next, we investigate the impact of the pixel masks  $\mu_1, \dots, \mu_m$ . To this end we consider three different settings, showcased in Fig. 3: (i) the full image ( $\ell_\infty$ -mask as before;  $m = 1$ ), (ii) “center + border” ( $m = 2$ ), where we consider the  $6 \times 6$  center pixel as one group and all others as another, and (iii) the  $2 \times 2$  grid ( $m = 4$ ) where we split the image into equally sized quarters. During template generation, we find the value of  $\epsilon_i$  via binary search for each  $\mu_i$ .

As we can see in Table 3, for higher  $m$  more patches can be matched to the templates, indicating that our optimization procedure is a good approximation to Problem 2. However, as  $m > 1$  methods are only marginally better than the  $\ell_\infty$ -mask, verification time gained by these additional matches does not offset additional template creation time. Thus,  $m = 1$  result in a better trade-off. Based on this investigation we now, in Table 4, evaluate all networks and datasets using  $m = 1$  and template generation at layers 2 and 3. In all cases, we obtain a speed up between 1.2 to  $2 \times$ .

Dataset	Net	verif. acc. [%]	$t^{BL}$	$t^{PS}$	patch mat. [%]	patch verf. [%]
MNIST	7x200	81.0	2.10	<b>1.10</b>	94.1	97.0
	9x500	96.0	2.70	<b>1.32</b>	93.0	95.3
CIFAR	7x200	29.0	3.28	<b>2.45</b>	33.7	42.2
	9x500	28.0	5.48	<b>4.48</b>	34.2	60.9

Table 4:  $\mathcal{I}_{2 \times 2}$  patch verification with templates generated on the second and third layer using the  $\ell_\infty$ -mask. Verification times are given for the baseline  $t^{BL}$  and for applying proof sharing  $t^{PS}$  in seconds per image.

$r$	verif. [%]	splits verf. [%]	splits mat. [%]	$t^{BL}$	$t^{PS}$
4	73.0	87.3	73.1	3.06	<b>1.87</b>
6	91.0	94.8	91.0	9.29	<b>3.81</b>
8	93.0	95.9	94.2	20.64	<b>7.48</b>
10	95.0	96.5	94.9	38.50	<b>13.38</b>

Table 5:  $\pm 2^\circ$  rotation,  $\pm 10\%$  contrast and  $\pm 1\%$  brightness change split into  $r$  perturbations on 100 MNIST images. Verification rate, rate of splits matched and verified along with the run time of Zonotope  $t^{BL}$  and proof sharing  $t^{PS}$ .

## 5.2 Robustness against geometric perturbations

For the verification of geometric perturbations we take 100 images from the MNIST dataset and the 7x200 neural network from §5.1. As before we use Zonotope propagation and create templates at the second and third layers.

In Table 5, we consider an input specification with  $\pm 2^\circ$  rotation followed by a  $\pm 10\%$  contrast and  $\pm 1\%$  brightness change. To certify the input region we consider its overapproximation in the Box domain as considered in Balunovic et al. (2019), and split it into  $r$  splits. Here we use  $m = 1$ , a single template, with optimized  $\epsilon$ . We observe that as we increase  $r$ , verification rate increases, but also the speed ups between 1.6 to  $2.9 \times$  obtained from proof sharing.

Finally, we investigate the impact of the number of templates  $m$ . For this we consider a  $\pm 40^\circ$  rotation generated input region with  $n_S = 200$ . In Table 6 we evaluate this for  $m$  templates obtained from the  $\ell_\infty$  input perturbation around  $m$  equally spaced rotations, where we apply binary search to find  $\epsilon$ . Again we observe that while  $m > 1$  allows more templates matches. However, here the relative increase is much larger, thus making  $m = 3$  faster than  $m = 1$ .

## 5.3 Offline Template generation

Finally, we present results of the offline template generation method, outlined in App. B. As discussed in §3, to this end we utilize the training set to generate templates. Table 7 shows results for the verification of  $\mathcal{I}_\epsilon$  on the test set utilizing these templates. As in §5.1 and §5.2 we use Zonotope propagation as the baseline. We observe up to  $1.2 \times$  speedup. Interestingly, it is possible to match up to 60.6 % of relaxations for previously unseen inputs to templates.

Method	$m$	splits matched [%]	$t$ [s]
Baseline	-	-	11.79
Proof Sharing	1	38.0	9.15
	2	41.1	9.21
	3	58.5	<b>8.34</b>

Table 6:  $\pm 40^\circ$  rotation split into 200 perturbations evaluated on 100 MNIST. While the verification rate is just 15 %, but 82.1 % of individual splits can be verified.

$k$	shapes matched [%]			verification time [s]		
	$m = 1$	$m = 3$	$m = 25$	$m = 1$	$m = 3$	$m = 25$
$\epsilon = 0.05$						
3	7.8	15.0	30.5	284.27	274.26	257.77
4	20.1	38.9	59.0	280.44	268.97	258.02
3+4	21.3	36.0	60.6	275.31	260.95	<b>241.36</b>
$\epsilon = 0.10$						
3	5.4	10.6	21.2	285.76	278.94	266.85
4	15.6	30.5	47.7	285.15	274.82	266.62
3+4	16.3	31.5	49.2	280.49	269.90	<b>257.82</b>

Table 7: Template matching rate and verification time of the whole MNIST test set a 5x100 using up to  $m$  templates per label and layer pair. The baseline verification 292.13 s and 291.80 s for  $\epsilon = 0.05$  and  $\epsilon = 0.10$  respectively.

## 5.4 Discussion

Throughout this section we have shown that proof sharing leads to speed-ups. These speed-ups are largest when the templates are placed at early layers.

We now also remark on some challenges and potential for future work. An interesting challenge lies in handling convolutional neural networks as with convolutional layers only limited proof subsumption (or template matching) can be observed (see App. A). For this reason we can only match templates after the convolutional layers which can be too late in the network to realize speed-ups. Addressing this challenge is an interesting item for future investigation.

Further, currently robust neural networks are often limited in their (verified) accuracy which directly limits the (verified) accuracy achievable via proof sharing. However, we believe proof sharing as a concept is orthogonal to improvements in verification procedures.

## 6 Conclusion

We introduced the novel concept of proof sharing in the context of neural network verification. We showed how to instantiate this concept in both online and offline settings, achieving speedups of up to  $2 \times$  in the online setting and obtaining a generalization of 60% to unseen inputs in the offline setting. We believe that the ideas introduced in this work can serve as a solid foundation for exploring methods that effectively share proofs in neural network verification.

## References

- an, S. G. 2018. On the Effectiveness of Interval Bound Propagation for Training Verifiabl. *ArXiv preprint*, abs/1810.12715.
- Anderson, R.; Huchette, J.; Tjandraatmadja, C.; and Vielma, J. P. 2019. Strong Mixed-Integer Programming Formulations for Trained Neural Networks. In *Proc. Integer Programming and Combinatorial Optimization (IPCO)*, volume 11480 of *Lecture Notes in Computer Science*.
- Ashok, P.; Hashemi, V.; Kretínský, J.; and Mohr, S. 2020. DeepAbstract: Neural Network Abstraction for Accelerating Verification. In *Automated Technology for Verification and Analysis - 18th International Symposium, ATVA 2020, Hanoi, Vietnam, October 19-23, 2020, Proceedings*, volume 12302 of *Lecture Notes in Computer Science*.
- Bak, S.; and Duggirala, P. S. 2017. Simulation-equivalent reachability of large linear systems with inputs. In *International Conference on Computer Aided Verification*. Springer.
- Balunovic, M.; Baader, M.; Singh, G.; Gehr, T.; and Vechev, M. T. 2019. Certifying Geometric Robustness of Neural Networks. In *Advances in Neural Information Processing Systems 32: Annual Conference on Neural Information Processing Systems 2019, NeurIPS 2019, December 8-14, 2019, Vancouver, BC, Canada*.
- Biggio, B.; Corona, I.; Maiorca, D.; Nelson, B.; Srndic, N.; Laskov, P.; Giacinto, G.; and Roli, F. 2013. Evasion Attacks against Machine Learning at Test Time. In *ECML/PKDD (3)*, volume 8190 of *Lecture Notes in Computer Science*.
- Botoeva, E.; Kouvaros, P.; Kronqvist, J.; Lomuscio, A.; and Misener, R. 2020. Efficient Verification of ReLU-Based Neural Networks via Dependency Analysis. In *The Thirty-Fourth AAAI Conference on Artificial Intelligence, AAAI 2020, The Thirty-Second Innovative Applications of Artificial Intelligence Conference, IAAI 2020, The Tenth AAAI Symposium on Educational Advances in Artificial Intelligence, EAAI 2020, New York, NY, USA, February 7-12, 2020*.
- Bunel, R.; Turkaslan, I.; Torr, P. H. S.; Kohli, P.; and Mudigonda, P. K. 2018. A Unified View of Piecewise Linear Neural Network Verification. In *Advances in Neural Information Processing Systems 31: Annual Conference on Neural Information Processing Systems 2018, NeurIPS 2018, December 3-8, 2018, Montréal, Canada*.
- Cheng, C.; and Yan, R. 2021. Continuous Safety Verification of Neural Networks. In *Design, Automation & Test in Europe Conference & Exhibition, DATE 2021, Grenoble, France, February 1-5, 2021*.
- Chiang, P.; Ni, R.; Abdelkader, A.; Zhu, C.; Studer, C.; and Goldstein, T. 2020. Certified Defenses for Adversarial Patches. In *Proc. of ICLR*.
- Dvijotham, K.; Stanforth, R.; Goyal, S.; Mann, T. A.; and Kohli, P. 2018. A Dual Approach to Scalable Verification of Deep Networks. In *Proceedings of the Thirty-Fourth Conference on Uncertainty in Artificial Intelligence, UAI 2018, Monterey, California, USA, August 6-10, 2018*.
- Dvijotham, K. D.; Stanforth, R.; Goyal, S.; Qin, C.; De, S.; and Kohli, P. 2019. Efficient Neural Network Verification with Exactness Characterization. In *Proceedings of the Thirty-Fifth Conference on Uncertainty in Artificial Intelligence, UAI 2019, Tel Aviv, Israel, July 22-25, 2019*, volume 115 of *Proceedings of Machine Learning Research*.
- Ehlers, R. 2017. Formal Verification of Piece-Wise Linear Feed-Forward Neural Networks. In *Automated Technology for Verification and Analysis - 15th International Symposium, ATVA 2017, Pune, India, October 3-6, 2017, Proceedings*, volume 10482 of *Lecture Notes in Computer Science*.
- Fischer, M.; Baader, M.; and Vechev, M. T. 2020. Certified Defense to Image Transformations via Randomized Smoothing. In *Advances in Neural Information Processing Systems 33: Annual Conference on Neural Information Processing Systems 2020, NeurIPS 2020, December 6-12, 2020, virtual*.
- Gehr, T.; Mirman, M.; Drachler-Cohen, D.; Tsankov, P.; Chaudhuri, S.; and Vechev, M. T. 2018. AI2: Safety and Robustness Certification of Neural Networks with Abstract Interpretation. In *2018 IEEE Symposium on Security and Privacy, SP 2018, Proceedings, 21-23 May 2018, San Francisco, California, USA*.
- Gurobi Optimization, L. 2020. Gurobi Optimizer Reference Manual.
- Katz, G.; Barrett, C. W.; Dill, D. L.; Julian, K.; and Kochenderfer, M. J. 2017. Reluplex: An Efficient SMT Solver for Verifying Deep Neural Networks. In *Computer Aided Verification - 29th International Conference, CAV 2017, Heidelberg, Germany, July 24-28, 2017, Proceedings, Part I*, volume 10426 of *Lecture Notes in Computer Science*.
- Katz, G.; Huang, D. A.; Ibeling, D.; Julian, K.; Lazarus, C.; Lim, R.; Shah, P.; Thakoor, S.; Wu, H.; Zeljić, A.; Dill, D. L.; Kochenderfer, M. J.; and Barrett, C. 2019. The Marabou Framework for Verification and Analysis of Deep Neural Networks. In *Proc. Computer Aided Verification (CAV)*.
- Krizhevsky, A.; Hinton, G.; et al. 2009. Learning multiple layers of features from tiny images.
- Krizhevsky, A.; Sutskever, I.; and Hinton, G. E. 2012. ImageNet Classification with Deep Convolutional Neural Networks. In *Advances in Neural Information Processing Systems 25: 26th Annual Conference on Neural Information Processing Systems 2012. Proceedings of a meeting held December 3-6, 2012, Lake Tahoe, Nevada, United States*.
- LeCun, Y.; Boser, B. E.; Denker, J. S.; Henderson, D.; Howard, R. E.; Hubbard, W. E.; and Jackel, L. D. 1989. Handwritten Digit Recognition with a Back-Propagation Network. In *Advances in Neural Information Processing Systems 2, [NIPS Conference, Denver, Colorado, USA, November 27-30, 1989]*.
- Li, L.; Weber, M.; Xu, X.; Rimanic, L.; Kailkhura, B.; Xie, T.; Zhang, C.; and Li, B. ????
- Lu, J.; and Kumar, M. P. 2020. Neural Network Branching for Neural Network Verification. In *Proc. of ICLR*.
- Maaten, L. v. d.; and Hinton, G. 2008. Visualizing data using t-SNE. *Journal of machine learning research*, 9(Nov).

- Madry, A.; Makelov, A.; Schmidt, L.; Tsipras, D.; and Vladu, A. 2018. Towards Deep Learning Models Resistant to Adversarial Attacks. In *Proc. of ICLR*.
- Mirman, M.; Gehr, T.; and Vechev, M. T. 2018. Differentiable Abstract Interpretation for Provably Robust Neural Networks. In *Proc. of ICML*, volume 80 of *Proceedings of Machine Learning Research*.
- Mohapatra, J.; Weng, T.; Chen, P.; Liu, S.; and Daniel, L. 2020. Towards Verifying Robustness of Neural Networks Against A Family of Semantic Perturbations. In *2020 IEEE/CVF Conference on Computer Vision and Pattern Recognition, CVPR 2020, Seattle, WA, USA, June 13-19, 2020*.
- Papernot, N.; McDaniel, P. D.; and Goodfellow, I. J. 2016. Transferability in Machine Learning: from Phenomena to Black-Box Attacks using Adversarial Samples. *ArXiv preprint*, abs/1605.07277.
- Paszke, A.; Gross, S.; Massa, F.; Lerer, A.; Bradbury, J.; Chanan, G.; Killeen, T.; Lin, Z.; Gimelshein, N.; Antiga, L.; Desmaison, A.; Köpf, A.; Yang, E.; DeVito, Z.; Raison, M.; Tejani, A.; Chilamkurthy, S.; Steiner, B.; Fang, L.; Bai, J.; and Chintala, S. 2019. PyTorch: An Imperative Style, High-Performance Deep Learning Library. In *Advances in Neural Information Processing Systems 32: Annual Conference on Neural Information Processing Systems 2019, NeurIPS 2019, December 8-14, 2019, Vancouver, BC, Canada*.
- Paulsen, B.; Wang, J.; and Wang, C. 2020. ReluDiff: differential verification of deep neural networks. In *ICSE '20: 42nd International Conference on Software Engineering, Seoul, South Korea, 27 June - 19 July, 2020*.
- Paulsen, B.; Wang, J.; Wang, J.; and Wang, C. 2020. NEURODIFF: Scalable Differential Verification of Neural Networks using Fine-Grained Approximation. In *35th IEEE/ACM International Conference on Automated Software Engineering, ASE 2020, Melbourne, Australia, September 21-25, 2020*.
- Pei, K.; Cao, Y.; Yang, J.; and Jana, S. 2017. Towards Practical Verification of Machine Learning: The Case of Computer Vision Systems. *ArXiv preprint*, abs/1712.01785.
- Raghunathan, A.; Steinhardt, J.; and Liang, P. 2018. Semidefinite relaxations for certifying robustness to adversarial examples. In *Advances in Neural Information Processing Systems 31: Annual Conference on Neural Information Processing Systems 2018, NeurIPS 2018, December 3-8, 2018, Montréal, Canada*.
- Roth, V.; Laub, J.; Kawanabe, M.; and Buhmann, J. M. 2003. Optimal Cluster Preserving Embedding of Nonmetric Proximity Data. *IEEE Trans. Pattern Anal. Mach. Intell.*, 25(12).
- Sadraddini, S.; and Tedrake, R. 2019. Linear Encodings for Polytope Containment Problems. In *58th IEEE Conference on Decision and Control, CDC 2019, Nice, France, December 11-13, 2019*.
- Salman, H.; Yang, G.; Zhang, H.; Hsieh, C.; and Zhang, P. 2019. A Convex Relaxation Barrier to Tight Robustness Verification of Neural Networks. In *Advances in Neural Information Processing Systems 32: Annual Conference on Neural Information Processing Systems 2019, NeurIPS 2019, December 8-14, 2019, Vancouver, BC, Canada*.
- Singh, G.; Gehr, T.; Mirman, M.; Püschel, M.; and Vechev, M. T. 2018a. Fast and Effective Robustness Certification. In *Advances in Neural Information Processing Systems 31: Annual Conference on Neural Information Processing Systems 2018, NeurIPS 2018, December 3-8, 2018, Montréal, Canada*.
- Singh, G.; Gehr, T.; Mirman, M.; Püschel, M.; and Vechev, M. T. 2018b. Fast and Effective Robustness Certification. In *Advances in Neural Information Processing Systems 31: Annual Conference on Neural Information Processing Systems 2018, NeurIPS 2018, December 3-8, 2018, Montréal, Canada*, 10825–10836.
- Singh, G.; Gehr, T.; Püschel, M.; and Vechev, M. T. 2019. An abstract domain for certifying neural networks. *PACMPL*, 3(POPL).
- Szegedy, C.; Zaremba, W.; Sutskever, I.; Bruna, J.; Erhan, D.; Goodfellow, I. J.; and Fergus, R. 2014. Intriguing properties of neural networks. In *Proc. of ICLR*.
- Tjeng, V.; Xiao, K. Y.; and Tedrake, R. 2019. Evaluating Robustness of Neural Networks with Mixed Integer Programming. In *Proc. of ICLR*.
- Tran, H.-D.; Lopez, D. M.; Musau, P.; Yang, X.; Nguyen, L. V.; Xiang, W.; and Johnson, T. T. 2019. Star-based reachability analysis of deep neural networks. In *International Symposium on Formal Methods*. Springer.
- Wang, S.; Pei, K.; Whitehouse, J.; Yang, J.; and Jana, S. 2018. Efficient Formal Safety Analysis of Neural Networks. In *Advances in Neural Information Processing Systems 31: Annual Conference on Neural Information Processing Systems 2018, NeurIPS 2018, December 3-8, 2018, Montréal, Canada*.
- Wei, T.; and Liu, C. 2021. Online Verification of Deep Neural Networks under Domain or Weight Shift. *ArXiv preprint*, abs/2106.12732.
- Weng, T.; Zhang, H.; Chen, H.; Song, Z.; Hsieh, C.; Daniel, L.; Boning, D. S.; and Dhillon, I. S. 2018. Towards Fast Computation of Certified Robustness for ReLU Networks. In *Proc. of ICML*, volume 80 of *Proceedings of Machine Learning Research*.
- Wong, E.; and Kolter, J. Z. 2018. Provable Defenses against Adversarial Examples via the Convex Outer Adversarial Polytope. In *Proc. of ICML*, volume 80 of *Proceedings of Machine Learning Research*.
- Zhang, H.; Weng, T.; Chen, P.; Hsieh, C.; and Daniel, L. 2018. Efficient Neural Network Robustness Certification with General Activation Functions. In *Advances in Neural Information Processing Systems 31: Annual Conference on Neural Information Processing Systems 2018, NeurIPS 2018, December 3-8, 2018, Montréal, Canada*.
- Zhong, Y.; Ta, Q.; Luo, T.; Zhang, F.; and Khoo, S. 2021. Scalable and Modular Robustness Analysis of Deep Neural Networks. *ArXiv preprint*, abs/2108.11651.

# Supplementary Material for Shared Certificates for Neural Network Verification

## A Properties of Robustness Proofs

In App. A.1 we investigate further variants of proof subsumption and provide technical details in App. A.2.

### A.1 Proof Similarity

It was established by (Krizhevsky, Sutskever, and Hinton 2012) that for semantically similar inputs  $\mathbf{x}$  and  $\mathbf{z}$ ,  $N_{1:k}(\mathbf{x})$  and  $N_{1:k}(\mathbf{z})$  are close in Euclidean norm. We showcase this hypothesis in Fig. 4a where activations at the fifth layer of a CNN of semantically similar inputs appear visually closer together. For technical details see App. A.2. Further, layers deeper in extract more abstract features, this similarity is expected to increase.

We lift these hypothesis from concrete points to sets of points (represented by relaxations obtained from a verifier): For semantically similar inputs  $\mathbf{x}$ ,  $\mathbf{y}$ , where  $\mathcal{I}(\mathbf{x})$  and  $\mathcal{I}(\mathbf{y})$  are certified as robust,  $N_{1:k}(\mathcal{I}(\mathbf{x}))$  and  $N_{1:k}(\mathcal{I}(\mathbf{y}))$  are numerically similar (their projections in many dimensions overlap). This overlap increases with the layer  $k \in \{1, \dots, L\}$  for an  $L$ -layer network.

In Fig. 4b, we depict the activations at layer  $k$  (blue dots in figure) for the six similar '2's shown in Fig. 4a. The blue region around each dot visualizes the Box (Gehr et al. 2018; Mirman, Gehr, and Vechev 2018; an 2018) abstract shape at the given layer (projected onto two dimensions), obtained by propagating  $\mathcal{I}_\epsilon(\mathbf{x})$  (with  $\epsilon = 0.1$ ). The figure illustrates that the shapes do overlap in two dimensions, and indeed our experiments confirm significant overlap when we consider all dimensions. We note that relaxations that incur more imprecision than others, naturally show higher overlap. We thus restrict our hypothesis to inputs  $\mathbf{x}$  for which  $\mathcal{I}(\mathbf{x})$  as (i) we ultimately want to argue about successful proofs rather than failed ones and (ii) for non-verifiable proofs the statement is trivial, as the intermediata relaxations can span the whole space of actions. This further suggests that, starting from an intermediate layer  $k$ , relaxations obtained from similar inputs can share their proofs for the remaining part of the network. Which is similar to the proof subsumption outlined in §3. Here, we now investigate another consequence.

As the relaxations of several similar inputs are so similar it is natural to assume that their convex hull (we will use the smallest approximation containing the convex hull) can also be verified when propagated through the neural network. We illustrate this in Fig. 4b which shows the projection of the approximation containing all regions in red. This red region may contain more points than the union of points found in the individual regions, yet one can still verify it as robust.

We now experimentally establish: (i) similar inputs produce similar relaxations, i.e. ones that substantially overlap and (ii) often the convex hulls of such relaxations are also verifiable.

[%]	$o_p^k$					$c_{0.9}^k$	
	1	2	3	4	5	4	5
$\epsilon = 0.1, p = 0.9$							
Similar	6	5	21	70	88	2	6
Class rand.	0	0	1	9	14	0	1
Random	0	0	0	0	1	0	0
$\epsilon = 0.2, p = 0.99$							
Similar	4	9	36	80	92	3	8
Class rand.	0	0	0	2	6	0	1
Random	0	0	1	2	3	0	0

Table 8: Overlap and containment of box verification for 5x100 on pairs of semantically similar inputs, pairs of random inputs of the same class, and randomly sampled inputs.

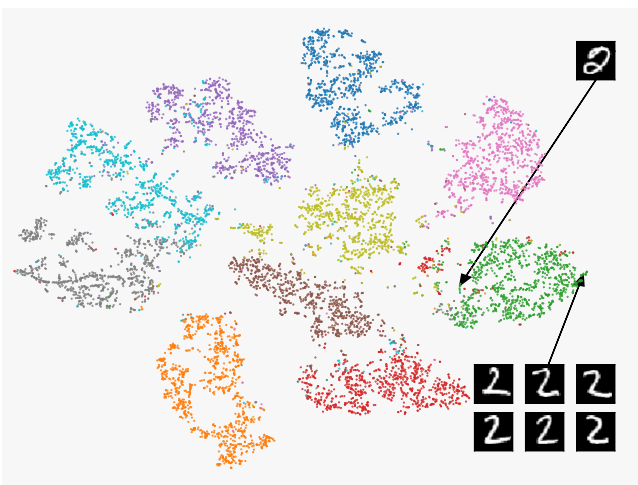
[%]	$o_p^k$						$c_{0.9}^k$
	1	2	3	4	5	6	6
$\epsilon = 0.1, p = 0.9$							
Similar	100	7	2	1	22	43	2
Class rand.	99	0	0	0	0	1	0
Random	94	0	0	0	0	1	0
$\epsilon = 0.2, p = 0.99$							
Similar	15	0	0	1	31	69	5
Class rand.	1	0	0	0	2	14	1
Random	0	0	0	0	0	2	0

Table 9: Overlap and containment of box verification for the CNN on pairs of semantically similar inputs, pairs of random inputs of the same class, and randomly sampled inputs.

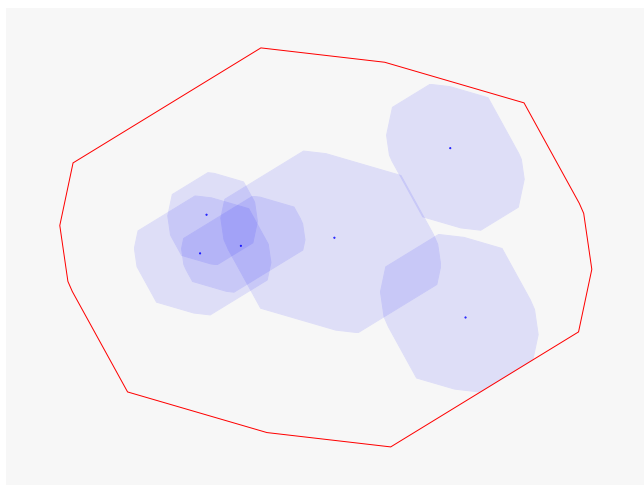
**Similar inputs produce similar relaxations** First we show that semantically similar inputs regions produce intermediate relaxations which overlap significantly.

We consider  $\mathcal{I}_\epsilon$  verification using the Box relaxation on robustly trained (Mirman, Gehr, and Vechev 2018) neural networks for handwritten digit (LeCun et al. 1989) classification. We consider two neural networks, a five layer feed forward neural network (with 100 neurons each), 5x100, as well as a convolutional neural network (CNN) (details in App. A.2). Further, we consider semantic similarity as closeness (in Euclidean distance) at intermediate layers (same metric as Krizhevsky, Sutskever, and Hinton (2012)). For a pair of two relaxations at a layer  $k$  with  $d$  dimensions, we consider two similarity indicators:

- $o_p^k$ , which indicates the percentage of inputs for which the relaxations in layer  $k$  overlap in at least  $p \cdot d$  (for  $p \in [0, 1]$ ).
- $c_p^k$ , which indicates the percentage of inputs for which one relaxation contains at least  $p \cdot d$  dimensions of the



(a) Activations at intermediate layer  $h$  of a neural network that classifies the MNIST (LeCun et al. 1989) handwritten digits. Inputs of the same label are colored the same. The 2-dimensional representation is obtained via a TSNE (Maaten and Hinton 2008) embedding, which aims to preserve the relative  $\ell_2$  distance between points. Thus semantically similar points are close together.



(b) Dots show activations at layer  $h$  for the six similar '2's (left). The blue regions outline the relaxations obtained from propagating  $\mathcal{I}_\epsilon(\mathbf{x})$  for each of them using the Box relaxation (Mirman, Gehr, and Vechev 2018; an 2018). The red outline shows the box tightly containing all relaxations. The two-dimensional representation is obtained via principal component analysis.

Figure 4: (left) low dimensional representation of the activation patterns at an intermediate layer in a handwritten digit classifier. Semantically similar inputs are clustered together. The six images of the digit '2' at the bottom are neighbors (both in projected and high dimensional space). They display similar styles of two, while distant points display other styles. (right) shows the activations for the same 6 images (blue dots) along with the region captured by propagating small perturbations using the Box relaxation. We provide technical details in App. A.2.

other at layer  $k$  (for  $p \in [0, 1]$ ).

In Tables 8 and 9 we provide the average of these metrics for pairs of semantically similar inputs, random pairs from the same class and completely random pairs. For the random inputs we sample 200 verifiable inputs from the test set and then consider all  $\binom{200}{2}$  possible pairs. For the class conditional random inputs we do the same but only sample from one class. In order to obtain similar inputs, we first pick 1000 verifiable inputs  $\mathbf{x}$ . For each, we then find their 5 closest semantic neighbors via the  $\ell_2$  distance of their concrete activations in an intermediate layer  $k$  (we use  $k = 4$  for 5x100 and  $k = 5$  for the CNN) and then discard those that are not verifiable. This results in a set  $X_{\mathbf{x}}$  of up to 6 verifiable inputs. We then consider all possible pairs of two in this set. The results in Tables 8 and 9 consider the relaxation pre-ReLU in each layer. The activations after the ReLU show the same trend, but inflate the overlap numbers due to many dimensions being set to zero. For the 5x100 network, in Table 8, we observe significant overlap for similar inputs and much lower overlap for randomly selected pairs. This result confirms what is to be expected from prior results on concrete activations (Krizhevsky, Sutskever, and Hinton 2012; Szegedy et al. 2014).

Interestingly for the CNN, in Table 9, we see high overlap  $o_p^1$  in the first layer, which happens as in the first convolution the error bounds for all inputs covered by the convolutional kernel are added, resulting in very large shapes. In subsequent convolutional layers as the activations diversify and the

Net	$\epsilon$	$ X_{\mathbf{x}} $	verif. [%]	#H
5x100	0.1	5.77	97	0.01
5x100	0.2	5.56	96	0.00
CNN	0.1	5.82	94	0.40
CNN	0.2	5.68	94	0.18

Table 10: Average size of  $X_{\mathbf{x}}$ , whether the union could be verified and how many half-space constraints (on average) were required to do so.

overlap drops before the expected pattern emerges.

### Convex hulls of intermediate relaxations are verifiable

Next we show that convex hulls of intermediate relaxations for similar input regions are verifiable. To this end we consider the  $X_{\mathbf{x}}$ , defined in the previous paragraph, and compute the join – the smallest shape in the convex relaxation that approximates their convex hull— over these sets, as standard:  $\bigsqcup(\{N_{1:k}(\mathcal{I}_\epsilon(\mathbf{x})) \mid \mathbf{x} \in X_{\mathbf{V}}\})$ . We then attempt to verify these unions using an exact verifier (Tjeng, Xiao, and Tedrake 2019) implemented in Gurobi (Gurobi Optimization 2020) and up to additional 30 half-space constraints as outlined in App. B.2. We show results in Table 10. From the size  $|X_{\mathbf{x}}|$  (close to 6) we observe that on average most inputs are verifiable and that indeed most unions are verifiable. For these small regions, especially on 5x100, only few half-space constraints are needed.

While in Table 8 we only rarely saw containment  $c_p^l$  we

Layer	Shape
Input	1x28x28
Convolution ( $k=3, s=1, p=1$ )	32x28x28
Convolution ( $k=4, s=2, p=1$ )	32x14x14
Convolution ( $k=3, s=1, p=1$ )	64x14x14
Convolution ( $k=4, s=2, p=1$ )	64x7x7
Flatten	3136
Linear	512
Linear	512
Linear	10

Table 11: Architecture of the ConvBig network. All convolution layers and all but the last linear layers apply the ReLU function. The parameters for the convolutions are the kernel size  $k$ , stride  $s$  and padding  $p$ . The architecture does not allow for templates at earlier layers (the convolutional layers are too wide to make template generation computationally feasible)

now see that even many of these relaxed convex hulls are verifiable.

## A.2 Technical Details

The 5x100 and CNN ‘‘ConvBig’’ (architecture described in Table 11) networks used in §3 and App. A.1 are obtained pretrained from Mirman, Gehr, and Vechev (2018), trained for provable robustness. The 5x100 network has an accuracy of 0.94 and a certified accuracy of 0.93 and 0.92 for  $\epsilon = 0.1$  and  $\epsilon = 0.2$  respectively. For the CNN these numbers are 0.93, 0.91 and 0.88.

In Fig. 4a we show the post-ReLU activations, with 512 dimensions, in the fifth hidden layer of CNN. The two dimensional embedding is obtained via TSNE embedding (Maaten and Hinton 2008), initialized with a 150-dimensional principal component analysis (PCA).

In Fig. 4b projection to two dimensions was obtained by applying (PCA) to the activation vectors of the 6 displayed points. The obtained linear projection operator was then applied to the relaxations. The red outline (their box join) was verified using exact verification - no half-space constraints were added.

Fig. 1b uses the same setup as used here to show proof subsumption, and the same PCA as Fig. 4b.

## B Offline Proof Sharing

After discussing template generation in an online manner (see §4) we now consider the offline setting. Here, we consider an instantiation of Problem 2, in the setting where  $\mathbf{x} \sim \mathcal{D}$  is drawn from the data distribution. As standard in machine learning, we assume that we have access to a large sample from  $\mathcal{D}$ , the training set  $T_{\text{train}}$ . We create  $\mathcal{T}$  offline from the training set, and then verify new inputs  $\mathbf{x}$  by utilizing  $\mathcal{T}$ . An important challenge here is that we require the templates  $\mathcal{T}$  to be general enough to generalize to unseen inputs.

**Running Example** As a running example we consider the simple feed forward neural network  $N$  with ReLU activations, shown in Fig. 5, consisting of four layers: an input layer, two hidden layers and an output layer with two neurons each. An affine transform followed by a *ReLU* is applied in the hidden layers, the last layer only applies the affine transform. Values are propagated left-to-right by multiplying them by the weight on the edge and then summing over all edges entering a node and adding the bias term denoted next to the node. Next, the ReLU (denoted  $R$ ) function is applied to this sum in the hidden layers. In a classification setting, the class with the highest output is considered the predicted class. We let  $\mathbf{x}$ ,  $h_1(\mathbf{x})$ ,  $h_2(\mathbf{x})$  and  $N(\mathbf{x})$  denote the input, the activations in the first and second hidden layer and the output of the neural network, respectively. That is,  $h_k$  is a shorthand for  $N_{1:k}$ .

Here we consider a perturbation  $\mathcal{I}_\epsilon$ , specifying  $\ell_\infty$ -noise of magnitude  $\epsilon = 0.5$ , and our goal will be to show that the whole input region  $\mathcal{I}_\epsilon(\mathbf{x})$  certifiably classifies to class 0, that is,  $N_1(\mathcal{I}_\epsilon(\mathbf{x})) > N_2(\mathcal{I}_\epsilon(\mathbf{x}))$  (meaning any value in the set that the first output neuron can take is strictly greater than any value in the set that the second output neuron can take).

To illustrate the concepts, we use the simple Box relaxation for propagating  $\mathcal{I}_\epsilon(\mathbf{x})$  where  $\begin{pmatrix} [a,b] \\ [c,d] \end{pmatrix}$  denotes a vector where the first component lies between  $a$  and  $b$  and the second between  $c$  and  $d$ . For ease of notation, we apply the functions  $h_1$ ,  $h_2$  and  $N$  to points as well as boxes, assuming the standard Box arithmetic.

For inputs  $\mathbf{x}^1 = \begin{pmatrix} 0.5 \\ 0.5 \end{pmatrix}$  and  $\mathbf{x}^2 = \begin{pmatrix} 1 \\ 0 \end{pmatrix}$ , we show the corresponding propagation of  $\mathcal{I}_\epsilon(\mathbf{x})$  in Fig. 5. Since all possible values for the second component of the output  $N(\mathcal{I}_\epsilon(\mathbf{x}))$  for  $\mathbf{x}^1$  and  $\mathbf{x}^2$  ( $[-2, 2]$  and  $[-1, 0]$ , respectively) are less than the lower bound of the first component (2.5 for both inputs) we can verify that the classification for both inputs is robust. Similarly, we can show that the same robustness property holds for a new input  $\mathbf{x}^3 = \begin{pmatrix} 1.5 \\ 0.5 \end{pmatrix}$ .

Comparing the proofs for  $\mathbf{x}^1$  and  $\mathbf{x}^3$  we note that at the second hidden layer we have  $h_2(\mathcal{I}_\epsilon(\mathbf{x}^3)) \subseteq h_2(\mathcal{I}_\epsilon(\mathbf{x}^1))$  (as  $[0, 1] \subseteq [0, 2]$ ) even though  $\mathcal{I}_\epsilon(\mathbf{x}^3) \not\subseteq \mathcal{I}_\epsilon(\mathbf{x}^1)$ . Thus, if we have already proved correct classification for  $\mathcal{I}_\epsilon(\mathbf{x}^1)$ , we can reuse this proof after asserting  $h_2(\mathcal{I}_\epsilon(\mathbf{x}^3)) \subseteq h_2(\mathcal{I}_\epsilon(\mathbf{x}^1))$ , as a result shortcutting the verification of  $\mathbf{x}^3$ .

*Proof Transfer between inputs* However, containment such as above is rare in practice and often only happens in deeper layers, thus diminishing gains from proof transfer. Thus, to obtain benefits, we need to somehow apply proof transfer earlier in the network. For our example, assume we are trying to verify  $\mathbf{x}^3$  and let us consider the first hidden layer  $h_1$ . Fig. 5 shows these relaxations distinctly colored, while Fig. 6 depicts them geometrically in the corresponding colors. We observe that  $h_1(\mathcal{I}_\epsilon(\mathbf{x}^3))$  is not contained in  $h_1(\mathcal{I}_\epsilon(\mathbf{x}^1))$  or  $h_1(\mathcal{I}_\epsilon(\mathbf{x}^2))$ . However, following our observations from App. A.1, we can compute the smallest box containing the two shapes, that is,  $T_1 = h_1(\mathcal{I}_\epsilon(\mathbf{x}^1)) \sqcup h_1(\mathcal{I}_\epsilon(\mathbf{x}^2))$  and obtain the template  $T_1$ , shaded in red in Fig. 6. Here,  $\sqcup$  denotes the join (operation computing the smallest box containing both operands). Propagating  $T_1$  further through the network allows us to successfully

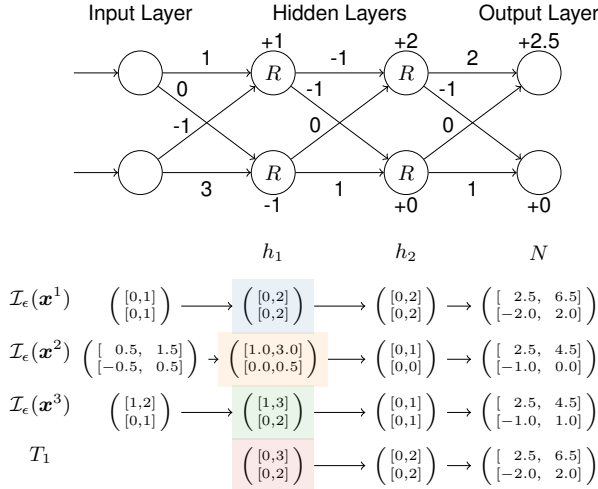


Figure 5: Feed forward network  $N$  with hidden layer activations  $h_1, h_2$ . Inputs are propagated left to right along the edges, multiplied with the weight along the edge and summed in the next node, where the bias shown below or above the node is added and the ReLU activation function  $R(t) = \text{ReLU}(t) := \max(t, 0)$  is applied.

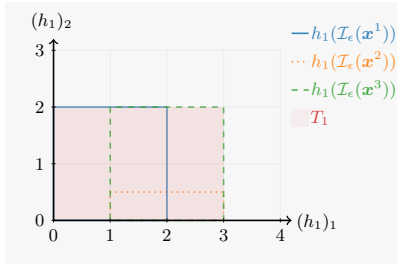


Figure 6: Relaxations the first hidden layer  $h_1$ . The dimensions are shown on the  $x$  and  $y$ -axis respectively.

verify that the classification is robust even if  $T_1$  is the intermediate output.  $T_1$  region includes  $h_1(\mathcal{I}_e(\mathbf{x}^3))$  and can thus be used to shortcut its verification at the first hidden layer. This showcases how we can create templates for previously unseen data points. Like this, in App. B.1, we compute templates offline on the training set, allowing for faster verification of new inputs.

To illustrate the speed-up expected from proof transfer, consider a feed forward neural network with  $L$  layers and  $n$  neurons each. Verification using Box relaxations then has a time complexity of  $\mathcal{O}(Ln^2)$ . If we create a template at layer  $k < L$ , and the template contains the input region propagated to layer  $k$ , then the complexity is reduced to  $\mathcal{O}(kn^2)$  plus a linear term for checking template containment. Crucial to obtaining end-to-end speed-ups is that the cost of the containment check does not exceed the gains from stopping the propagation at layer  $k$ . In case the template is not sufficient to prove the given input region, the full verification must be computed by further propagating from layer  $k$  to the end. Suppose that the constructed template contains the proof for a given input with a probability

$\rho$ , then the overall complexity of our verification procedure is  $\mathcal{O}((\rho k + (1 - \rho)L)n^2)$  in expectation. It can be observed that the gains in obtained speedup increase with  $\rho$ .

## B.1 Template Generation on Training Data

We first outline the template generation process in general and then show an instantiation for  $\ell_\infty$ -robustness verification in App. B.2.

**Template Generation** We first consider the creation of templates where our aim is to verify a single  $\mathcal{I}$  over new points in the data distribution, e.g. the test set. Then present an extension to multiple  $\mathcal{I}_1, \dots, \mathcal{I}_r$ . Assuming a sufficiently large  $T_{\text{train}}$ , where we obtain verification rate  $\mathbb{E}_{\mathbf{x} \in T_{\text{train}}} [N(\mathcal{I}(\mathbf{x})) \vdash \psi]$ , we can theoretically construct  $\mathcal{T}$  containing all relaxations observed at layer  $k$  by propagating all  $\mathcal{I}(\mathbf{x})$  and taking their possible convex unions. We would then, due to the properties outlined in App. A, expect to obtain similar verification rates when using  $\mathcal{T}$  to certify new input regions. However, in practice this rate will be diminished by the size of  $T_{\text{train}}$ , the limit  $|\mathcal{T}| \leq m$  on the number of allowed templates (which we add to allow for efficient template matching, Problem 3) and by how well the proof subsumption properties holds in practice on the considered network and input regions.

Thus, in order to optimize Eq. (1) under our constraints, we attempt to find the set of templates  $\mathcal{T}$  that contains the most relaxations at layer  $k$  obtained from  $T_{\text{train}}$ . While this is generally computationally hard, we approximate this with a clustering-based approach. To this end, we first compute the relaxations  $N_{1:k}(\mathcal{I}(\mathbf{x}))$  for  $\mathbf{x} \in T_{\text{train}}$  and then cluster and merge them. Subsequently, we further merge the obtained templates until we obtain a set  $\mathcal{T}$  of  $m$  templates. We formalize the template generation procedure in Algorithm 3 and showcase it in Fig. 7.

We first (line 1, Fig. 7a) compute the set  $\mathcal{V}$  of relaxation at layer  $k$ , that can be verified. Then, we cluster the relaxations in  $\mathcal{V}$  into  $n$  groups  $\mathcal{G}_i$  of similar relaxations using the function `cluster_shapes` (which we will instantiate in App. B.2), showcased by different colors in Fig. 7b. For each group  $\mathcal{G}_i$ , we compute its convex hull  $T$  via the join operator  $\sqcup$ . The join returns a (usually the tightest) expressible shape in the chosen relaxation that includes all its inputs. If we verify this  $T$ , then we add the tuple  $(T, \mathcal{G}_i)$ , the template along with all relaxations it covers, to the set  $\mathcal{H}$ , shown in Fig. 7c. As depicted in Fig. 7d, we attempt to merge pairs of these templates (line 12). To this end, we traverse them in order of their distance  $d$ . Here, we use the Euclidean distance between the centers of  $T_1$  and  $T_2$  for  $d(T_1, T_2)$ . In order to merge  $(T_1, \mathcal{G}_1)$  and  $(T_2, \mathcal{G}_2)$ , we first compute the set of their contained shapes  $\mathcal{G}' = \mathcal{G}_1 \cup \mathcal{G}_2$  (line 13) and then again compute the join  $T' = \sqcup(\mathcal{G}')$  (line 14). If  $T'$  can be verified, we replace  $(T_1, \mathcal{G}_1)$  and  $(T_2, \mathcal{G}_2)$  by  $(T', \mathcal{G}')$  in  $\mathcal{H}$  (lines 15 to 21). This procedure is repeated until no templates can be merged. Finally,  $\mathcal{T}$  is obtained as the set of the  $m$  templates with the most associated relaxations (e.g., the largest  $|\mathcal{G}|$ ) in  $\mathcal{H}$ .

A potentially more optimal set  $\mathcal{T}$  (in terms of relaxations contained) could be found by adding  $\mathcal{H} \leftarrow \mathcal{H} \cup$

---

**Algorithm 3:** Template generation over  $T_{\text{train}}$ 

---

**Input:** training set  $T_{\text{train}}$   
**Result:** Set  $\mathcal{T}$  of templates,  $|\mathcal{T}| \leq m$

- 1  $\mathcal{V} \leftarrow \{N_{1:k}(\mathcal{I}(\mathbf{x})) \mid \mathbf{x} \in T_{\text{train}}, N(\mathcal{I}(\mathbf{x})) \vdash \psi\}$
- 2  $\mathcal{G}_1, \dots, \mathcal{G}_n \leftarrow \text{cluster\_shapes}(\mathcal{V})$
- 3  $\mathcal{H} \leftarrow \emptyset$
- 4 **for**  $i \leftarrow 1$  **to**  $n$  **do**
- 5      $T \leftarrow \sqcup_D(\mathcal{G}_i)$
- 6     **if**  $N_{k+1:L}(T) \vdash \psi$  **then**
- 7          $\mathcal{H} \leftarrow \mathcal{H} \cup \{(T, \mathcal{G}_i)\}$
- 8     **end**
- 9 **end**
- 10  $\text{pairs} \leftarrow$  all pairs  $(T_1, \mathcal{G}_1), (T_2, \mathcal{G}_2)$  in  $\mathcal{H}$
- 11  $Q \leftarrow$  priority queue over pairs, ordered by  $d(T_1, T_2)$
- 12 **foreach** pair  $(T_1, \mathcal{G}_1), (T_2, \mathcal{G}_2)$  in  $Q$  **do**
- 13      $\mathcal{G}' = \mathcal{G}_1 \cup \mathcal{G}_2$
- 14      $T' = \sqcup_D(\mathcal{G}')$
- 15     **if**  $N_{k+1:L}(T') \vdash \psi$  **then**
- 16          $\mathcal{H} \leftarrow \mathcal{H} \setminus \{(T_1, \mathcal{G}_1), (T_2, \mathcal{G}_2)\}$
- 17         remove elements containing  $(T_1, \mathcal{G}_1)$  from  $Q$
- 18         remove elements containing  $(T_2, \mathcal{G}_2)$  from  $Q$
- 19         add all pairs  $(T, \mathcal{G}), (T', \mathcal{G}')$  for  $(T, \mathcal{G}) \in \mathcal{H}$   
           to  $Q$
- 20          $\mathcal{H} \leftarrow \mathcal{H} \cup \{(T', \mathcal{G}')\}$
- 21     **end**
- 22 **end**
- 23  $\mathcal{T} \leftarrow T$  for  $(T, \mathcal{G}) \in \mathcal{H}$  for the  $m$  largest  $|\mathcal{G}|$
- 24 **return**  $\mathcal{T}$

---

$\{(\alpha(P), \{P\}) \mid N_{k+1:L}(\alpha(P)) \vdash \psi, P \in \mathcal{G}_i\}$  if verification of  $T$  generated from  $\mathcal{G}_i$  in line 6 fails. Here  $\alpha(P)$  denotes the conversion of a relaxation in one parameterization (e.g., Zonotope) to another (e.g. Box). While formally this could be any such conversion (called an abstraction operator) when we instantiate this in App. B.2, we use the same Zonotope to Box conversion as in §4. This way, the iterative template merge between lines 10 and 21 could compute a more optimal solution. However, as this is generally computationally infeasible, we refrain from doing so.

**Extension to multiple  $\mathcal{I}_1, \dots, \mathcal{I}_r$ .** So far in this section we assumed a single  $\mathcal{I}$ . However, the same algorithm can be applied to multiple  $\mathcal{I}_1, \dots, \mathcal{I}_r$ . Depending on the similarity of the perturbations, a set of templates  $\mathcal{T}_1, \dots, \mathcal{T}_r$  can be obtained for each perturbation by applying Algorithm 3 separately or a joint  $\mathcal{T}$  by either merging them afterwards or by instantiating  $\mathcal{V}$  in line 1 with  $\mathcal{V} \leftarrow \{N_{1:k}(\mathcal{I}(\mathbf{x})) \mid \mathbf{x} \in T_{\text{train}}, N(\mathcal{I}_i(\mathbf{x})) \vdash \psi, i \in \{1, \dots, r\}\}$ .

After finding templates in this manner we then perform an additional step called *template extension*, discussed in App. B.3, in which we linearly enlarge the obtained template.

## B.2 Dataset templates for $\ell_\infty$ robustness

We now instantiate the template generation algorithm for  $\ell_\infty$ -robustness verification  $\mathcal{I}_e$ . As in §4, we propagate specifications as Zonotopes and represent templates as Boxes.

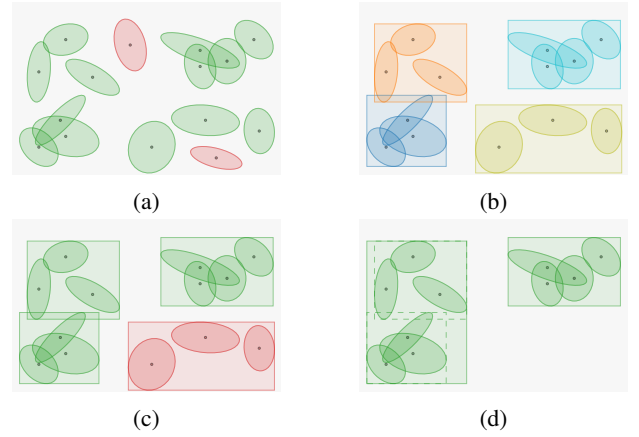


Figure 7: Visualization of Algorithm 3. First, in (a) the relaxations at layer  $k$  for input regions in the training set are obtained, and restricted to the verifiable ones (green). These are then clustered and their convex hulls in domain  $D$  are obtained. (b) shows different clusters in different colors. The convex hulls are then verified (c), and restricted to the verifiable ones (green). Finally in (d), these regions are further merged, if possible, to obtain the set of templates.

For the verification of the templates (lines 6 and 15) we perform exact verification via Mixed-Integer Linear Programming (MILP) (Tjeng, Xiao, and Tedrake 2019). The box-encoded templates can be directly verified by the exact verifier. We note that since exact verification is strictly more precise than Zonotope propagation, the use of templates can potentially allow for *higher* certification rates than directly employing Zonotope propagation. While we did not observe this experimentally, it presents an interesting target for further investigation.

We now briefly outline the properties of exact verification, as we require these in the following discussion. The framework from Tjeng, Xiao, and Tedrake (2019), proves classification to the correct label  $l$  by maximizing the error  $e = \max_{i \neq l} \mathbf{n}_i - \mathbf{n}_l$  (asserting that  $e < 0$ ), where  $\mathbf{n}$  denotes the output of the neural network (e.g. its logits) over the considered input region. If no counterexample to that assertion can be found, it certifies the specification, else it returns a set of counterexamples  $\{z_{V,i}\}$  (concrete points in the input region), utilized later, for which this error is maximal. In both cases we can access value  $e$  of the error function.

Next, we instantiate cluster\_shapes with  $k$ -means clustering for which we provide a similarity matrix computed as follows: for each pair  $P_1, P_2 \in \mathcal{V}$  we compute  $B = P_1 \sqcup_B P_2$ , where  $\sqcup_B$  denotes their Box join, and use  $\exp(e)$  as their distance, where  $e \in \mathbb{R}$  is the error obtained from exact verification when attempting to verify  $\psi$  for  $B$ . To obtain a similarity matrix from these distances, we apply a constant shift embedding (Roth et al. 2003). As invoking exact verification for each pair  $(P_1, P_2)$  is expensive, we only consider the  $t$  closest neighbors (in  $\ell_2$  distance between centers) and set all others to a maximal distance.

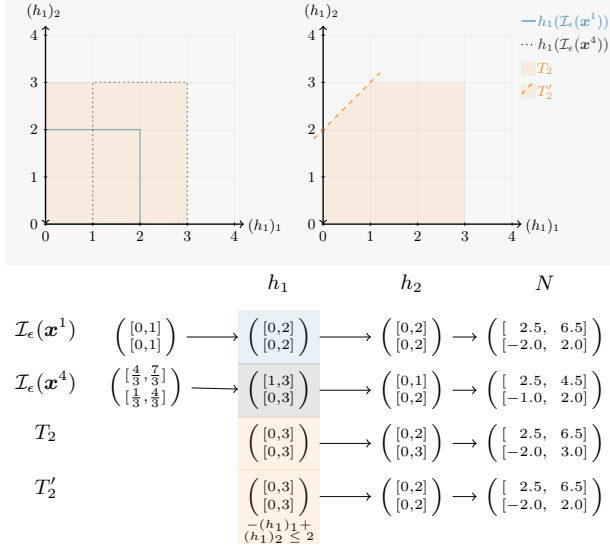


Figure 8: Continuation of the running example:  $T_2$  is not verifiable, yet  $T_2'$  with additional half-space constraint, is.

**Half-space constraints** To allow for larger templates  $T$ , e.g., those that allow to optimize Eq. (1) further by containing more relaxations, we extend the template representation from Boxes to Boxes with additional half-space constraints. The resulting convex polyhedra, formally called Stars (Tran et al. 2019; Bak and Duggirala 2017), allow for larger boxes while the half-space constraints cut-off potentially non-verifiable regions, yet, still allow efficient containment checks  $S \subseteq T$ .

Formally a Star  $B^S$  over a Box  $B$  is denoted as:

$$B^S(\mathbf{C}, \mathbf{c}) := \{z \in \mathbb{R}^d \mid z \in B \wedge \mathbf{C}z \leq \mathbf{c}\} \quad (4)$$

with  $\mathbf{C} \in \mathbb{R}^{c \times d}$ ,  $\mathbf{c} \in \mathbb{R}^c$ .

Here each half-space constraint is described by a hyperplane parameterized by  $\mathbf{C}_i$ . and  $c_i$ .

The containment check  $S \subseteq T^S$  for an relaxation  $S$ , e.g. a zonotope, and star  $T^S$  consists of: (i) a containment for the underlying box  $S \subseteq T$ , and (ii) checking if for each constraint  $\mathbf{C}_i \cdot z \leq c_i$ , maximizing the linear expression  $\mathbf{C}_i \cdot z$  with respect to  $S$  yields an objective  $\leq c_i$ . For a zonotope  $S$  as given in §4, we have shown the computation of step (i) in App. B.2 and can efficiently check step (ii) via  $\mathbf{C}\mathbf{a} + \sum_{j=1}^p |\mathbf{C}\mathbf{A}|_j \leq \mathbf{c}$ .

A star encoded as in Eq. (4) can be directly verified using exact verification (MILP) by adding the half-space constraints as further LP constraints. We now showcase the utility of these hyperplane constraints before describing their generation.

**Example (cont.)** We illustrate this in Fig. 8, as a continuation of our running example. The region  $T_2$ , shaded orange, is obtained by Box join  $T_2 = h_1(\mathcal{I}_\epsilon(\mathbf{x}^1)) \sqcup h_1(\mathcal{I}_\epsilon(\mathbf{x}^4))$ . While  $h_1(\mathcal{I}_\epsilon(\mathbf{x}^1))$  and  $h_1(\mathcal{I}_\epsilon(\mathbf{x}^4))$  are both verifiable,  $T_2$  is not. However, if we add a new half-space constraint given

by  $\mathbf{C} := \begin{pmatrix} 1, -1 \end{pmatrix}$  and  $\mathbf{c} := \begin{pmatrix} 2 \end{pmatrix}$ , the resulting template  $T_2'$  (a star) becomes verifiable.

**Obtaining half-space constraints** In the template generation process we utilize Boxes as before. However, whenever we fail to verify a template (e.g., lines 6 and 15 in Algorithm 3), we attempt to add a half-space constraint. We repeat this up to  $n_{\text{hs}}$  times resulting in as many constraints. We leverage the exact verifier for obtaining half-space constraints. Recall, that it either verifies a region or provides a set of counterexamples  $\{z_{V,i}\}$ . Since we only add additional half-space constraints, if the verification fails we utilize these counterexamples. In the following we assume a single  $z_V$ , which in practice is usually the case, and derive a hyperplane that separates  $z_V$  from the relaxation we are trying to verify. If there are multiple  $z_{V,i}$ , we iterate over them and perform the described procedure for each  $z_{V,i}$ , that is not already cut by the hyperplane found for a previous counterexample. These hyperplanes directly yield the new constraints.

We showcase this in Fig. 9, where the green shaded area  $T$  shows the Box join over three relaxations  $T = \sqcup(\{P_1, P_2, P_3\})$ . The individual  $P_i$ , shown in blue, are zonotopes, that can be verified individually. .

The verification of the green area fails, with the counterexample  $z_V$  (red dot) shown in the top right corner. To find a hyperplane that separates  $z_V$  from the rest of  $T$ , we consider the line from the center  $\mathbf{a}$  (green dot) of  $T$  to the point  $z_V$  and a hyperplane orthogonal to it (shown as the dashed line). Thus, adding a row  $i$  to the matrix  $\mathbf{C}$  of the star:  $\mathbf{C}_i = (z_V - \mathbf{a})^T$ . To find offset  $\mathbf{h} = \lambda \mathbf{a} + (1 - \lambda)z_V$  (for  $\lambda \in [0, 1]$ ) along this line to, we consider the value attained for  $\mathbf{C}_i \mathbf{x}$  for  $\mathbf{x}$  in the verified area ( $P_1, P_2, P_3$ ):

$$c_p := \max_{P \in \{P_1, P_2, P_3\}} \max_{\mathbf{x} \in P} \mathbf{C}_i \mathbf{x}.$$

Then, the constant  $c_i$  of the new hyperplane is given by  $c_i = \kappa c_p + (1 - \kappa)c_z$  for a hyper-parameter  $\kappa$  and  $\mathbf{z}_z := \mathbf{C}_i \mathbf{z}_V$ .

A high  $\kappa$  puts the hyperplane close to  $z_V$ , removes only little volume from the template, while low  $\kappa$  puts it closer to  $\mathbf{a}$ . Since  $z_V$  is only the counterexample with the largest violation, but not necessarily the whole region preventing certification, the half-space constraint obtained from a high  $\kappa$  might not be sufficient to separate this region from  $T$ . Thus, in a subsequent iteration, another half-space constraint for the same region may be added. For low  $\kappa$ , fewer constraints are required, but more verifiable volume of  $T$  is lost. Based on these considerations we outline our choices of  $\kappa$  in App. C.2.

### B.3 Template Expansion

To further improve the generalization from the training set to the test set, we introduce an operation called *template expansion*, outlined in Algorithm 4. For the scaling operation we utilize a diagonal matrix  $\mathbf{D} := \text{diag}(f_1, \dots, f_d)$ , where  $f_i \geq 1$  is the scaling factor for the  $i$ -th dimension, e.g.  $\mathbf{D} = 1.1\mathbf{I}$  would scale all dimensions by a factor 1.1.

**Example (cont.)** We illustrate this by extending the running example in Fig. 10. On the left in Fig. 10, tem-

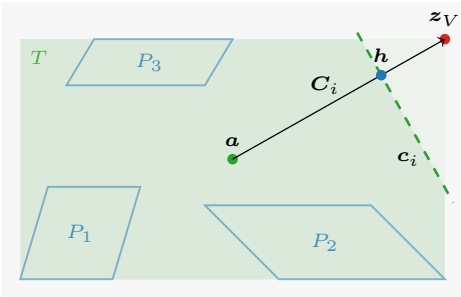


Figure 9: The algorithm used to find half-space constraints, by cutting counterexample  $z_V$  from the template  $T$  with a hyperplane ( $C_i, c_i$ ). The normal of the hyperplane (specified by  $C_i$ ) is given by the vector between  $a$  (the center of  $T$ ) and  $z_V$ . The threshold  $c_i$  is chosen such that the hyperplane remove  $z_V$  but does not intersect any relaxations  $P_1, P_2, P_3$  the template  $T$  was created from.

---

**Algorithm 4:** Template expansion

---

**Input:**  $\mathcal{T} = \{T_i\}_{i=1}^m$ , scaling matrix  $D$

**Result:** Set  $\mathcal{T}$  of expanded templates,  $|\mathcal{T}| = m$

```

1 for  $i \leftarrow 1$  to  $k$  do
2    $T \leftarrow T_i$ 
3   while  $N_{k+1:L}(T) \vdash \psi$  do
4      $T_i \leftarrow T$ 
5     scale all dimensions of  $T$  according to  $D$ 
6   end
7 end
8 return  $\mathcal{T} = \{T_i\}_{i=1}^m$ 

```

---

plate  $T_1$  (shaded red) is obtained as before and the relaxation  $h_1(\mathcal{I}_\epsilon(x^5))$  for a new input  $x^5$ , is shown in purple.  $h_1(\mathcal{I}_\epsilon(x^4))$  overlaps with template  $T_1$  but is not contained inside it.

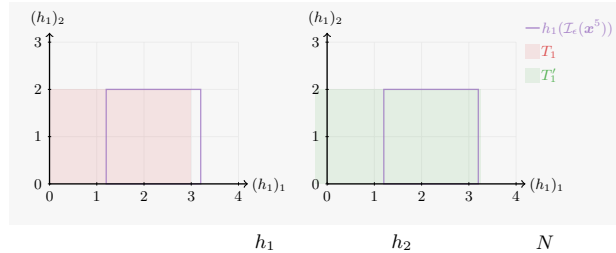
By applying template expansion with  $D = \text{diag}(\frac{7}{6}, 1)$ , we obtain the template  $T'_1$ , shaded in green on the right of Fig. 10.  $T'_1$  can be verified and now also contains  $h_1(\mathcal{I}_\epsilon(x^5))$ , thus allowing to shortcut the verification of  $\mathcal{I}_\epsilon(x^5)$ .

We note that in this case one loop iteration of Algorithm 4 was performed (as expanding  $T'_1$  further would yield a non-verifiable shape).

**Half-space Constraints** When we use the Box relaxation with half-space constraints (Stars) to encode templates, the expansion only modifies the underlying box, but not the half-space constraints, since these have already been selected to be close to the decision boundary. However, we attempt to add new constraints during the expansion process if the verification fails.

## B.4 Experimental Evaluation

Here we instantiate the presented algorithm App. B.2 for the MNIST dataset. We first consider templates expressed in the Box relaxation, and investigate Stars with additional half-space later. We generate the set of templates  $\mathcal{T}$  individually



$$\begin{aligned}
 \mathcal{I}_\epsilon(x^5) & \begin{pmatrix} [1.2, 2.2] \\ [0.0, 1.0] \end{pmatrix} \rightarrow \begin{pmatrix} [1.2, 3.2] \\ [0.0, 2.0] \end{pmatrix} \rightarrow \begin{pmatrix} [0.0, 0.8] \\ [0.0, 0.8] \end{pmatrix} \rightarrow \begin{pmatrix} [2.5, 4.1] \\ [-0.8, 0.8] \end{pmatrix} \\
 T_1 & \begin{pmatrix} [0, 3] \\ [0, 2] \end{pmatrix} \rightarrow \begin{pmatrix} [0, 2] \\ [0, 2] \end{pmatrix} \rightarrow \begin{pmatrix} [2.5, 6.5] \\ [-2.0, 2.0] \end{pmatrix} \\
 T'_1 & \begin{pmatrix} [-0.25, 3.25] \\ [0.00, 2.00] \end{pmatrix} \rightarrow \begin{pmatrix} [0.00, 1.75] \\ [0.00, 2.25] \end{pmatrix} \rightarrow \begin{pmatrix} [2.50, 6.00] \\ [-1.75, 2.25] \end{pmatrix}
 \end{aligned}$$

Figure 10: Continuation of the running example showcasing the template expansion algorithm. While the template  $T_1$  does not subsume  $h_1(\mathcal{I}_\epsilon(x^5))$  the expanded template  $T'_1$  does.

for each label.

Here, we consider the 5x100 and CNN networks as in App. A (see App. A.2) and apply template generation individually per label. In the 5x100 we create templates at the third and fourth layers and for the CNN after the first linear layer. We create templates in the box as well as in the star relaxation and allow up to  $m = 25$  templates and use template expansion (App. B.3). For  $\epsilon = 0.05$  we found between 6 and 24 templates per label and layer for the 5x100.

Tables 12 and 13 show the results. A subset of these results has already been prefetched in Table 7 in §5. We provide the fraction of input regions that could be successfully matched to templates as well as the overall verification time. If an input cannot be matched with any of the templates, then we propagate the standard Zonotope relaxation through the rest of the network to verify it.

For the 5x100 FFNN we observe that templates can subsume up to 60.6% of input regions in the test set with  $\epsilon = 0.05$ , and up to 49.2% for higher  $\epsilon = 0.1$  when expressed in the Box relaxation. Combining template at multiple layers gives more matched templates as many inputs can be matched in the third layer, while unmatched ones can again be considered at the fourth layer. We observe that improvements in matching rate directly lead to speed ups over standard verification. Additionally allowing half-space constraints, that is use Stars instead of Boxes as templates, allows us to increase the matching rate up to 65.2 % and 54.5 % for the two  $\epsilon$  respectively. However, as checking matches for Stars is computationally more expensive the verification time does not improve further.

In the CNN we observe higher matching rates compared to the 5x100 network. However, here the difference in verification time in comparison to the standard verification is negligible. The reason for this is that we found templates to only work well in the linear layers, which are late in the architecture, thus diminishing run time gains. We observe strong correlation between accuracy, verified accuracy and the matching rates. Labels with higher accuracy also tend to

<b>Box</b>	shapes matched [%]			verification time [s]			
	$k$	$m = 1$	$m = 3$	$m = 25$	$m = 1$	$m = 3$	$m = 25$
$\epsilon = 0.05$							
3	07.5	14.4	28.4	$282.60 \pm 2.18$	$275.32 \pm 1.34$	$259.87 \pm 0.68$	
4	19.5	38.0	57.6	$279.87 \pm 0.07$	$270.08 \pm 0.81$	$258.06 \pm 1.23$	
3+4	20.7	39.3	59.2	$274.86 \pm 0.31$	$259.19 \pm 0.91$	$243.11 \pm 0.81$	
$\epsilon = 0.10$							
3	05.1	10.2	19.4	$286.67 \pm 1.17$	$280.45 \pm 1.03$	$272.01 \pm 0.68$	
4	15.0	29.6	45.8	$283.06 \pm 1.49$	$275.39 \pm 1.04$	$268.05 \pm 1.04$	
3+4	15.8	30.7	47.4	$281.14 \pm 1.12$	$272.17 \pm 1.18$	$257.92 \pm 0.97$	
<b>Box+TE</b>							
	$k$	$m = 1$	$m = 3$	$m = 25$	$m = 1$	$m = 3$	$m = 25$
$\epsilon = 0.05$							
3	7.8	15.0	30.5	$284.27 \pm 0.63$	$274.26 \pm 1.78$	$257.77 \pm 1.21$	
4	20.1	38.9	59.0	$280.44 \pm 1.66$	$268.97 \pm 1.13$	$258.02 \pm 1.38$	
3+4	21.3	36.0	60.6	$275.31 \pm 2.62$	$260.95 \pm 0.70$	$241.36 \pm 1.34$	
$\epsilon = 0.10$							
3	5.4	10.6	21.2	$285.76 \pm 0.71$	$278.94 \pm 1.12$	$266.85 \pm 2.07$	
4	15.6	30.5	47.7	$285.15 \pm 0.47$	$274.82 \pm 1.41$	$266.62 \pm 0.45$	
3+4	16.3	31.5	49.2	$280.49 \pm 0.70$	$269.90 \pm 0.34$	$257.82 \pm 3.01$	
<b>Star</b>							
	$k$	$m = 1$	$m = 3$	$m = 25$	$m = 1$	$m = 3$	$m = 25$
$\epsilon = 0.05$							
3	10.8	25.2	40.4	$281.33 \pm 1.44$	$269.24 \pm 1.30$	$254.41 \pm 0.87$	
4	25.8	40.3	62.7	$282.51 \pm 2.10$	$281.68 \pm 0.60$	$271.63 \pm 0.89$	
3+4	27.9	45.1	64.3	$277.89 \pm 1.38$	$266.55 \pm 0.93$	$246.39 \pm 0.31$	
$\epsilon = 0.10$							
3	7.9	18.2	29.0	$284.31 \pm 2.19$	$277.96 \pm 0.60$	$267.72 \pm 0.85$	
4	20.2	31.9	51.0	$285.68 \pm 2.10$	$286.16 \pm 0.79$	$278.29 \pm 1.30$	
3+4	21.7	35.8	52.9	$283.43 \pm 0.91$	$278.00 \pm 0.60$	$262.96 \pm 1.04$	
<b>Star+TE</b>							
	$k$	$m = 1$	$m = 3$	$m = 25$	$m = 1$	$m = 3$	$m = 25$
$\epsilon = 0.05$							
3	11.1	25.8	41.8	$282.99 \pm 0.45$	$271.34 \pm 1.89$	$254.62 \pm 1.05$	
4	25.9	40.6	63.6	$282.98 \pm 1.46$	$281.51 \pm 0.23$	$270.44 \pm 0.30$	
3+4	28.3	45.6	65.2	$278.00 \pm 0.36$	$269.08 \pm 0.80$	$247.43 \pm 0.09$	
$\epsilon = 0.10$							
3	8.1	18.7	30.3	$285.82 \pm 1.91$	$280.71 \pm 2.99$	$267.55 \pm 0.77$	
4	20.3	32.3	52.8	$285.49 \pm 1.04$	$286.34 \pm 0.79$	$276.14 \pm 0.30$	
3+4	22.0	36.2	54.5	$284.39 \pm 2.29$	$278.90 \pm 0.34$	$262.60 \pm 1.71$	

Table 12: Extended version of Table 7. Template matching rate and verification time of the whole MNIST test set  $t$  in seconds for the 5x100 using up to  $m$  templates per label and layer pair. The baseline verification  $292.13 \pm 1.77$  and  $291.80 \pm 2.36$  seconds for  $\epsilon = 0.05$  and  $\epsilon = 0.10$  respectively. +TE indicates the use of Template Expansion.

label	acc [%]	verif. acc. [%]	verification time per image [s]					matching rates [%]			
			baseline	B <sup>-</sup>	B <sup>+</sup>	S <sup>-</sup>	S <sup>+</sup>	B <sup>-</sup>	B <sup>+</sup>	S <sup>-</sup>	S <sup>+</sup>
0	99	97	169.78 ± .9	168.64 ± .4	168.44 ± .4	173.34 ± .3	178.28 ± .6	50.0	52.2	75.1	81.0
1	98	96	186.35 ± .5	185.24 ± .1	184.45 ± .2	187.52 ± .3	191.16 ± .4	69.0	72.7	85.8	88.6
2	95	91	171.38 ± .2	171.22 ± .3	171.09 ± .4	174.60 ± .2	176.12 ± .4	36.9	40.0	65.5	66.4
3	94	89	165.83 ± .4	165.85 ± .0	165.84 ± .2	168.79 ± .2	177.47 ± .4	18.8	19.8	51.7	59.4
4	91	87	155.49 ± .3	155.50 ± .2	155.39 ± .2	158.37 ± .6	158.34 ± .2	18.1	20.8	52.2	53.4
5	94	88	147.08 ± .3	147.33 ± .2	147.21 ± .3	150.81 ± .0	152.17 ± .2	3.4	6.1	54.8	59.9
6	97	95	160.36 ± .4	159.99 ± .6	159.90 ± .3	164.38 ± .1	165.10 ± .2	44.9	47.8	75.7	78.9
7	89	84	158.38 ± .2	157.74 ± .1	157.35 ± .3	160.41 ± .5	161.88 ± .3	41.8	43.9	59.4	65.7
8	90	84	152.48 ± .4	152.93 ± .2	152.84 ± .2	155.58 ± .7	155.69 ± .2	15.9	16.6	40.0	42.9
9	88	82	153.11 ± .1	152.68 ± .3	152.89 ± .0	155.23 ± .8	156.68 ± .1	21.9	23.4	46.7	50.9

Table 13: Accuracy, certified accuracy for  $\epsilon = 0.1$  and verification time and matching rates for different template generation algorithms on the CNN Table 11. Templates are created after the first linear layer. The methods B and S refer to the box and star domain respectively. The latter describes boxes with additional half-space constraints. The additional superscripts +/- stand for template generation with/without template expansion.

have higher matching rates, with the difference in-between the labels being more significant for the latter. Adding half-space constraints to boxes allows them to have larger bounds and still be verifiable, with the half-space constraints truncating counterexamples from the templates. These stars can better approximate the decision boundaries, thereby increasing the number of matches on average from 35.2% to 65.1%. Unfortunately, this gain cannot be converted to a speed-up, due to the larger cost of the containment check for stars and the late template layer.

These results highlight, that with the algorithm outlined in App. B.2, a set of templates  $\mathcal{T}$  can be obtained that generalize remarkably well to new input regions (e.g., up to 65.2% containment). That is, while more precise relaxations such as stars allow templates that capture a far higher rate of containment for new input regions, their added cost of the containment check makes the obtained speedups smaller.

Finally, we see that in both the CNN and the 5x100 network Template Expansion (App. B.3) uniformly leads to a higher matching rate and speed-ups.

## C Experimental Details

### C.1 Details for §5

The neural networks was trained using robust training (Madry et al. 2018) for patch attacks, as outlined in (Chiang et al. 2020). The 7x200 and 9x500 networks were trained for 600 epochs to achieve accuracies on MNIST (LeCun et al. 1989) of 98.3% and 95.3% respectively. These same values for the CIFAR (Krizhevsky, Hinton et al. 2009) dataset a 48.8% and 48.1% respectively. Further numbers can be found in Table 4.

For Zonotope propagation we use the DeepZ algorithm (Singh et al. 2018b).

In §5.3 and App. B we use the same networks as in App. A (see App. A.2). When we use Zonotopes there, we use the ReLU propagation outlined in Mirman, Gehr, and Vechev (2018); Gehr et al. (2018), as this is more applicable to networks trained with Mirman, Gehr, and Vechev (2018).

Further details for §5.3 are given below.

### C.2 Details for App. B.4

For a cluster\_proofs we set an initial cluster size depending on the number of verifiable images per label, in order that the clusters contain on average 50 images. For the verification of a cluster’s union, we allow up to  $n_{\text{hs}} = 30$  half-space constraints and set  $\kappa$  of 0.05. Taking a low value leads to a larger truncation, but reduces the number of half-space constraints, which speeds up the template generation as well as the containment check at inference. We take the same values also for verifying unions after merging two clusters. For expanding the templates, we use up to 10 iterations, in which we widen by 5% in each dimension and then allow up to 10 hyperplanes to verify the expanded template. To avoid truncating previously verified volume, we increase  $\kappa$  linearly by 0.02 for each expansion step, starting with an initial  $\kappa$  of 0.4

## D Additional Results

### D.1 Standard deviations for Timings

In Tables 14–18 we report the standard deviation for the timings in §5. The standard deviations for Table 7 can be found in Table 12.

### D.2 Optimal Speedup

Finally, we want to determine the maximal possible speedup with proof sharing and see how much of this potential is realized by our method. To this end we investigate the setting in Table 2.

Table 19 shows the “optimal” speed-up achievable if Zonotopes are only propagated up to layer  $k$  (averaged over the same 100 inputs as in Table 2). If we further consider the cost for template generation (essentially the run time of Algorithm 1) as the average observed cost, which is 0.058, 0.055, 0.054 and 0.049 s for the considered layers respectively, this diminishes the achievable speedup. Another factor that decreases this speedup is the time for template matching, which is on average 0.036, 0.047, 0.048, 0.048 s when assuming 729 matches per layer.

The results show that our realized speedups for layers 3 and 4 are very close to the optimally achievable result, high-

$k$	verification time [s]								
	-	1	2	3	4	1+3	2+3	2+4	2+3+4
MNIST	$2.10 \pm 0.01$	$1.94 \pm 0.01$	$1.15 \pm 0.04$	$1.22 \pm 0.01$	$1.41 \pm 0.01$	$1.27 \pm 0.05$	<b><math>1.09 \pm 0.01</math></b>	$1.10 \pm 0.04$	$1.14 \pm 0.03$
CIFAR	$3.27 \pm 0.24$	$2.98 \pm 0.31$	$2.53 \pm 0.09$	$2.32 \pm 0.01$	$2.47 \pm 0.16$	$2.35 \pm 0.02$	$2.49 \pm 0.14$	<b><math>2.42 \pm 0.04</math></b>	$2.55 \pm 0.21$

Table 14: Extended version of Table 2.  $\mathcal{I}_{2 \times 2}$  patch verification for different combinations of template layers  $k$ , 7x200 networks, using  $m = 1$  template.

Method/Mask	m	patch matched [%]	$t$ [s]
Baseline	-	-	$2.14 \pm 0.10$
L-infinity	1	94.1	<b><math>1.11 \pm 0.05</math></b>
Center + Border	2	94.6	$1.41 \pm 0.01$
2x2 Grid	4	<b>95.0</b>	$3.49 \pm 0.06$

Table 15: Extended version of Table 3.  $\mathcal{I}_{2 \times 2}$  patch verification with templates at the 2nd & 3rd layer of the 7x200 networks for different masks.

Dataset	Net	verif. acc. [%]	$t^{BL}$	$t^{PS}$	patch mat. [%]	patch verif. [%]
MNIST	7x200	81.0	$2.10 \pm 0.01$	<b><math>1.10 \pm 0.03</math></b>	94.1	97.0
	9x500	96.0	$2.70 \pm 0.01$	<b><math>1.32 \pm 0.00</math></b>	93.0	95.3
CIFAR	7x200	29.0	$3.28 \pm 0.07$	<b><math>2.450.06</math></b>	33.7	42.2
	9x500	28.0	$5.48 \pm 0.03$	<b><math>4.48 \pm 0.03</math></b>	34.2	60.9

Table 16: Extended version of Table 4.  $\mathcal{I}_{2 \times 2}$  patch verification with templates generated on the second and third layer using the  $\ell_\infty$ -mask. Verification times are given for the baseline  $t^{BL}$  and for applying proof sharing  $t^{PS}$  in seconds per image.

$r$	verif. [%]	splits verif. [%]	splits mat. [%]	$t^{BL}$	$t^{PS}$
4	73.0	87.3	73.1	$3.06 \pm 0.01$	<b><math>1.87 \pm 0.01</math></b>
6	91.0	94.8	91.0	$9.29 \pm 0.01$	<b><math>3.81 \pm 0.01</math></b>
8	93.0	95.9	94.2	$20.64 \pm 0.05$	<b><math>7.48 \pm 0.01</math></b>
10	95.0	96.5	94.9	$38.50 \pm 0.05$	<b><math>13.38 \pm 0.02</math></b>

Table 17: Extended version of Table 5.  $\pm 2^\circ$  rotation,  $\pm 10\%$  contrast and  $\pm 1\%$  brightness change split into  $r$  perturbations on 100 MNIST images. Verification rate, rate of splits matched and verified along with the run time of Zonotope  $t^{BL}$  and proof sharing  $t^{PS}$ .

Method	$m$	splits matched [%]	$t$ [s]
Baseline	-	-	$11.79 \pm 0.05$
Proof Sharing	1	38.0	$9.15 \pm 0.01$
	2	41.1	$9.21 \pm 0.01$
	3	58.5	<b><math>8.34 \pm 0.01</math></b>

Table 18: Extended version of Table 6.  $\pm 40^\circ$  rotation split into 200 perturbations evaluated on 100 MNIST. While the verification rate is just 15 %, but 82.1 % of individual splits can be verified.

Layer $k$	speedup at layer $k$			
	1	2	3	4
optimal	4.57	2.90	2.13	1.69
optimal+gen	4.02	2.68	2.01	1.62
optimal+gen+match	3.75	2.51	1.92	1.56
realized	1.08	1.83	1.72	1.49

Table 19: Speedups achievable in the setting of Table 2. “optimal” shows the speedup that is achieved if Zonotopes are just propagated to layer  $k$ . “+gen” also takes into consideration the average time for template generation. “+match” further also considers the cost of template matching. Realized shows the actual speedup obtained in Table 2.

lighting the fit of the chosen template generation procedure. Results at earlier layers stray further from the optimum as we do not observe as high template matching rates there (and assume these to be unrealistic in practice).